Dead Sea

19-20.2.2009

Field leaders

Meir Abelson

Amir sagy

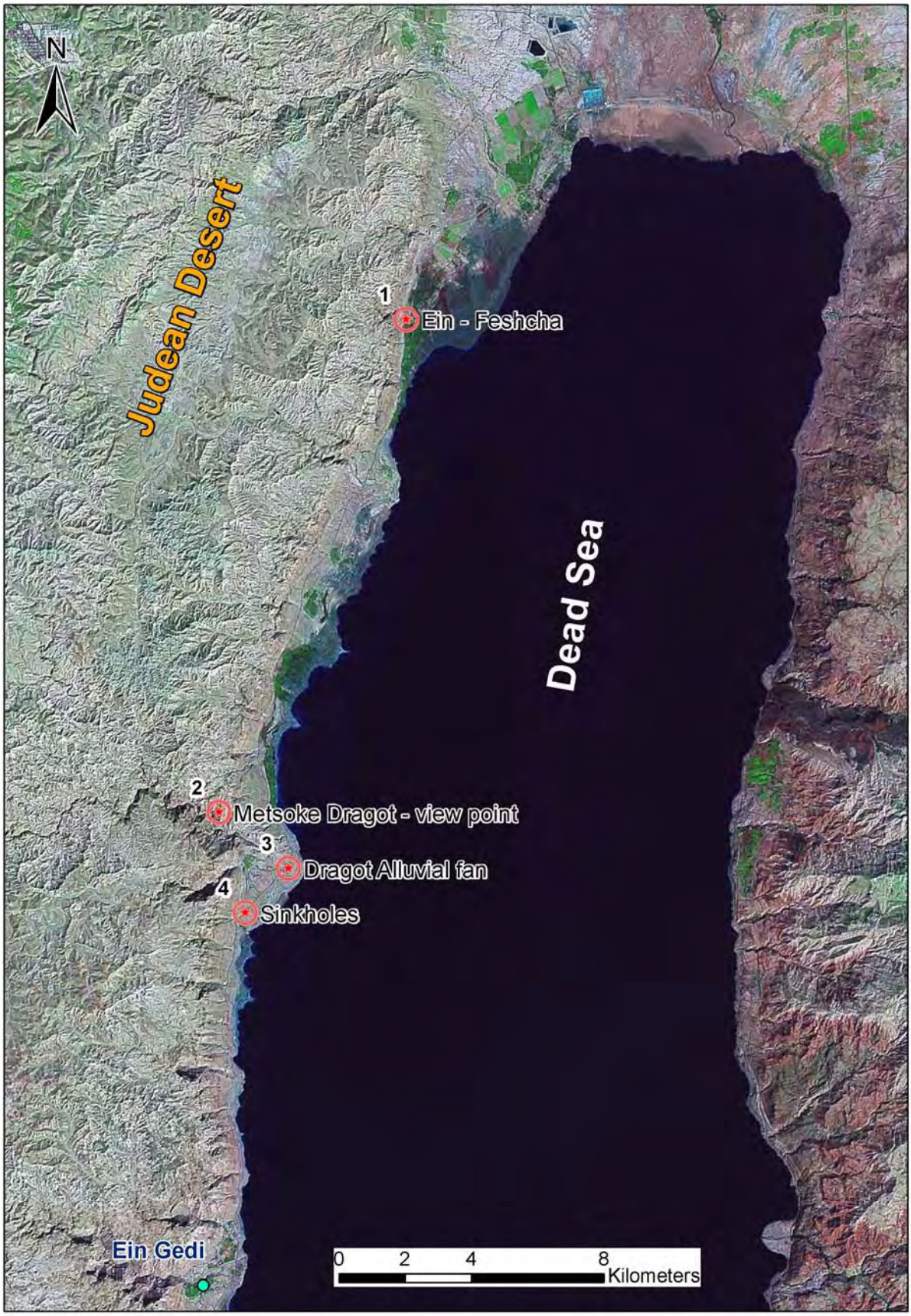
N
Judean Desert
1
Ein - Feshcha
Dead Sea
2
Metsoke Dragot - view point
3
Dragot Alluvial fan
4
Sinkholes
Ein Gedi
0 2 4 8
Kilometers

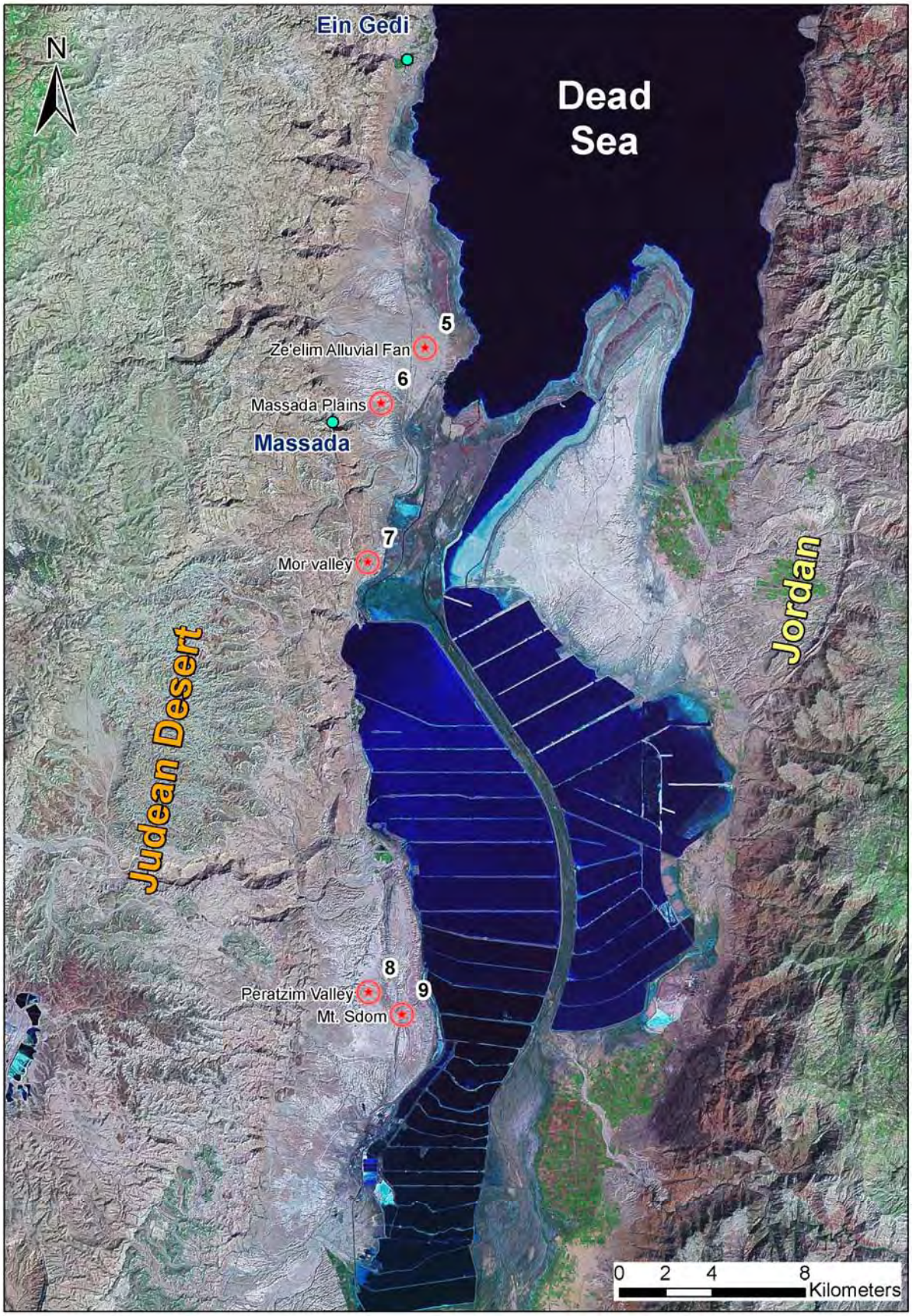
N
Ein Gedi
Dead Sea
5
Ze'elim Alluvial Fan
6
Massada Plains
Massada
7
Mor valley
Judean Desert
Jordan
8
Peratzim Valley
9
Mt. Sdom
0 2 4 8
Kilometers

Radon signals in geogas of the upper crust – The Enot Zuqim sector, NW Dead Sea

Gidi Steinitz[1*]

[1]Geological Survey of Israel

Steinitz @gsi.gov.il

[*]Field guide

Radon (^{222}Rn) is a radioactive inert gas formed by disintegration from ^{226}Ra as part of the ^{238}U decay series. It occurs at varying concentrations in geological environments. The combination of its noble gas character and its radioactive decay make it a unique ultra-trace component for tracking temporally varying natural processes in subsurface systems. Using nuclear techniques the measurement sensitivity for radon in the subsurface geogas is extremely high and can be performed with a time resolution in the order of 1 hour or less. The application of stress to rocks is thought to enhance the exhalation of radon from the solid mineral phase, rendering radon a potential sensitive tracer of geodynamic processes in the upper crust. Transport of radon in soil and water has been investigated as a tool for monitoring volcanic activity and the proposition that radon may serve as a useful proxy for seismic activity has been repeatedly raised. Radon is viewed in these scenarios as a highly sensitive tracer of secondary geodynamic processes – mainly mechanical and thermal. Despite the presumed advantages of radon as a geophysical proxy, the utilization of radon in geodynamics has been hampered by the complex patterns of the measured signals.

The research team at the Geological Survey of Israel is addressing, since 1990, the temporal variations of radon and its geophysical significance in geogas in upper crustal rocks in the frame of the Israel Geophysical Radon Project (IGRnP. Intensive high-time resolution (<1 hour) monitoring of Rn is being performed since 1995 in upper crustal rock systems, along the western margin of the Dead Sea transform (DST). Presently radon is being monitored in a 200 km segment along the western boundary fault of the DST, from the Dead Sea to the Gulf of Aqaba. Several arrays of stations, spanning 0.5 to 20 km, consist each of several monitoring sites (Table 1). The Rn signals are characterized by: a) unambiguous temporal signature types (Steinitz et al., 1992; Steinitz et al., 1996; Steinitz et al., 1999, Balogh and Steinitz, 2004); b) recurrence at the different locations within the same geologic unit; c) similar features recorded in diverse geographic, geological and geodynamic situations.

A large regional (20 km) and most intense (high level) radon flux anomaly is developed along the western fault scarp of the DST, in the Enot Zuqim (EZ) segment in NW sector of the Dead Sea. The anomaly occurs in the unconsolidated gravel from the fault scarp eastwards, to the shore of the Dead Sea. Several radon monitoring sites, spanning +15km and utilizing 15-minute sampling, are operative in the EZ. Site 17, situated along the active fault site and operative since 1995, is a world scale key locality in terms of the intensity of the recorded radon signals.

Temporal variations and signals of radon occur at the EZ sites. The signals are classified based on the temporal scale of the variation, as follows: a) Seasonal variation of radon (SR), periodic at 1 cycle/yr; b) Multi-Day (MD) signals, lasting 2-20 days, which are non-periodic; c) Diurnal Radon (DR) signals, which have typical periods of 24-, 12- and 8-hours (S1, S2, S3). Indicative gravity diurnal periodic constituents (M1, O1) are clearly lacking in the radon time series. This is interpreted to indicate that the DR signal (S1, S2, S3 constituents) is driven by a solar tide related process.

Using an 8-year record of Rn, obtained next to a major active boundary fault of the DST, a statistically significant relation between multi-day Rn signals and earthquakes in the nearby sector of the DSR was demonstrated by Steinitz et al. (2003). In these works the establishment of the geodynamic nature of the signatures and signals is based on negation of atmospheric influence, analyzing radon signatures in the geological, spatial, time and frequency domains and, primarily, on correlating radon with geophysical phenomena, and specifically the correlation to earthquakes (Steinitz et al., 2003; Begin and Steinitz, 2005).

Recent advance in the understanding of these radon phenomena is demonstrated by using the geophysical approach as applied for analysis of radon signal in the Elat Granite (by Steinitz et al., 2006, 2007). A new geophysical framework for the temporal patterns of radon is obtained by: i) applying advanced time series methods and signal processing approaches in the time and frequency domain to long (multi-year) and high-resolution (< 1 hour) radon time series for the extraction and description of the superimposed signals; ii) the analysis of the environmental and geophysical influences on radon time series; and iii) both multi-site and multi-parameter analysis of radon phenomena and other geophysical phenomena. The primary outcomes concerning the radon signal in the subsurface are: a) the compound variation is composed of a periodic Seasonal Radon (SR) signal, a periodic Daily Radon (DR) signal containing diurnal (24-hour) and semi-diurnal (12-hour) periods, and non-periodic Multi-Day (MD) signals; b) the MD signals may be representing transients of a mechanical affiliation; c) the SR and especially the DR signals are probably generated in the subsurface by a solar irradiance related process.

Table 1: Monitoring sites of the IGRnP, north to south along 200km sector of the DST

Region/Array (extent in km)	Site	Elev. (m)	Depth (m)	Geology		
				Age	lithology	Structural and tectonic situation
Enot Zuqim (EZ), NW Dead Sea (20 km)	19W	-388	2	Recent	Gravel	Along and next to active main western fault of the central segment of the DST
	19E	-368	2			
	17W	-373	2			
	23W	-381	2			
	23C	-364	2			
	23E	-364	2			
	21W	-364	2			
Ramon (GAV) (0.1 km)	GAV1.2	470	1.2	Lower Cretaceous	Syenite	Intraplate
	GAV85		85			
Southern Arava (0.1 km, each]	BGO	220	~ 80	Precambrian	Granite	Uplifted structural blocks along the western margin of the southern segment of the DST.
	RODED	285	10		Meta diorite	
Elat Granite (ELTGR) (1 km)	E1	29	10		Granite	
	E2	27	4			
	E3	53	53			
Gulf of Elat (0.1 km)	IUI	-1.5		Recent	Gravel, Seawater	Active main western fault of the DST

References

Balogh, B. and Steinitz, G., Radon monitoring at the Gavnunim site, Makhtesh Ramon. Interim Report. Isr. Geol. Surv. Tech. Rep. TR-GSI/22/04, 17p., 2004.

Barbosa, S. M., G. Steinitz, O. Piatibratova, M. E. Silva, and P. Lago, Radon variability at the Elat granite, Israel: Heteroscedasticity and nonlinearity, Geophys. Res. Lett., 34, L15309, 2007. doi:10.1029/2007GL030065.

Begin, Z.B. and Steinitz, G., Temporal and spatial variations of micro-earthquake activity along the Dead Sea Fault, 1984-2004. Israel Jour. Earth Sci., 54, 1-14, 2005.

Steinitz, G., Begin, Z.B. and Gazit-Yaari, N., A Statistically Significant Relation between Rn Flux and Weak Earthquakes in the Dead Sea Rift Valley. Geology, 31, 505-508, 2003.

Steinitz, G., O. Piatibratova, and S. M. Barbosa, Radon daily signals in the Elat Granite, southern Arava, Israel, J. Geophys. Res., 112, B10211, 2007. doi:10.1029/2006JB004817

Steinitz, G., Piatibratova, O., and Malik, U., Radon signals in the Elat Granite pluton, southern Arava, Israel. Geol. Surv. Rep. GSI/18/06, 53p., 2006.

Steinitz, G., Vulkan, U., Lang, B., Gilat, A. and Zafrir, H., Radon emanation along border faults of the Rift in the Dead Sea area. Israel Jour. Earth Sci., 41, 9-20, 1992.

Steinitz, G., Vulkan, U. and Lang, B., Monitoring of the tectonically related radon flux in Israel. Isr. Geol. Surv., Current Res., 10, 148-153, 1996.

Steinitz, G., Vulkan, U., Lang, B., The Radon flux at the northwestern segment of the Dead Sea (Dead Sea Rift) and its relation to earthquakes. Israel Jour. Earth Sci., 48, 283-299, 1999.

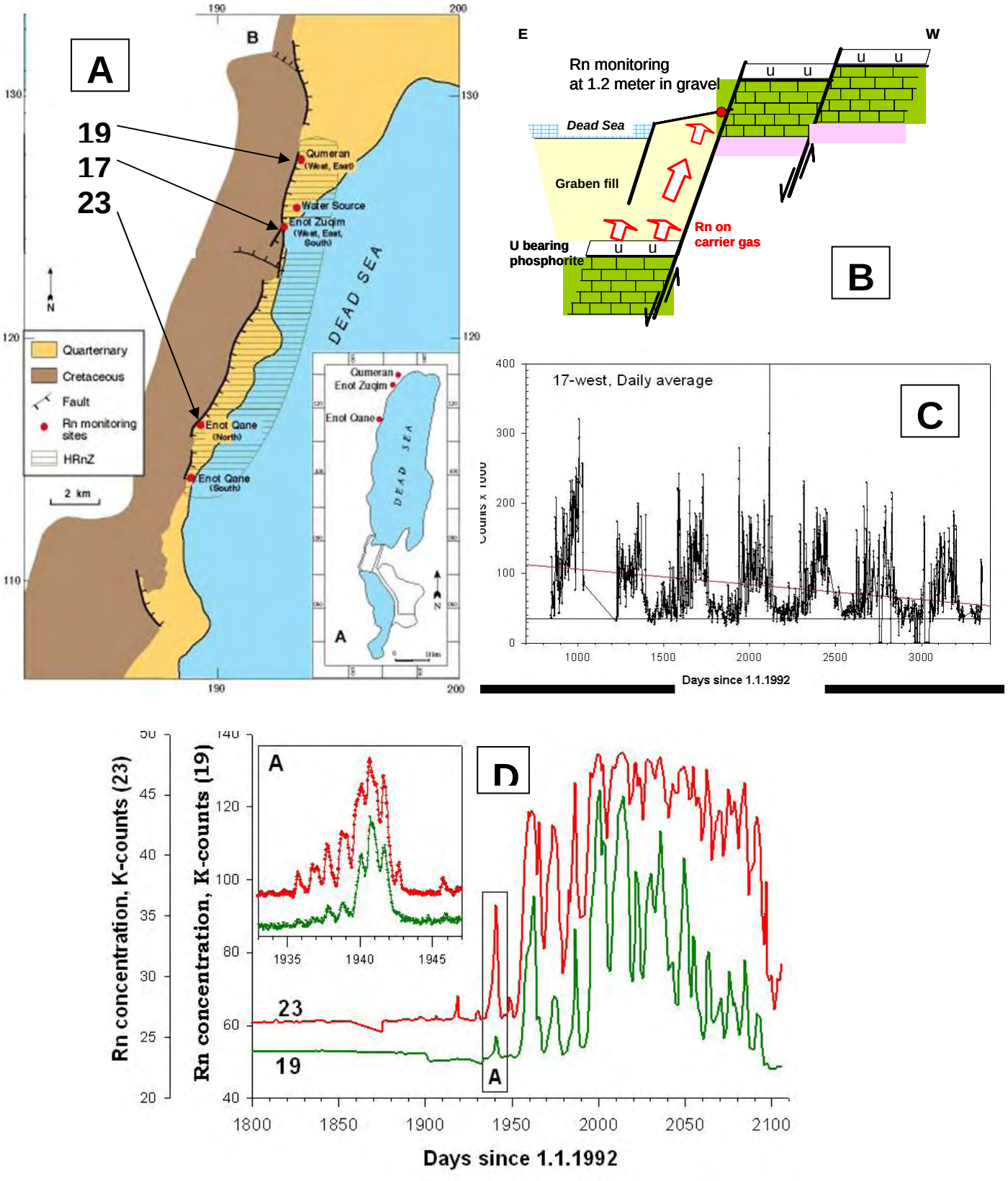

A – Regional radon anomaly along the fault scarp of the western boundary fault of the DST and location of radon high-time resolution monitoring sites in the unconsolidated gravel.

B – Schematic cross section, at the primary monitoring site 17W, presenting a possible model for the local radon flux regime.

C – Long term monitoring (+7 years) at site 17 showing: 1) a long term variation; 2) periodic annual radon signal, and 3) superimposed non periodic multi-day radon signals.

D – Radon time series at sites 19 & 23 showing regional correlation of: 1) annual radon signal; 2) superimposed non periodic multi-day radon signals, and 3) periodic diurnal signals (inset).

Active tectonics in the Nahal Darga Fan-Delta

Yehouda Enzel[1]*, Yehuda Eyal[2], Galit Kadan[2],

[1]The Hebrew University of Jerusalem
[2]Ben Gurion University of the Negev

yenzel@cc.huji.ac.il

* Field guide

In this site we will see large exposures into the Holocene fan-delta of Nahal Darga that is deposited on top one of the major faults in the western Dead Sea basin according to available data. Holocene and late Pleistocene fan-deltas are common features along the western margins of the Dead Sea (e.g., Sneh, 1979; Bowman, 1974; Manspeizer, 1985; Kadan, 1997; Bartov et al., 2006). Such fan-deltas can record the areal and temporal distribution of significant earthquakes (Sims, 1975; Dunne and Hempton, 1984; Allen, 1984). As the Darga fan is one of the largest and situated farther to the east than most other fans in the western margin, it probably forming over a major structure, at least as the faults are mapped (Fig. 1). Its very steep delta front and the nearby bathymetry support this association. In this station we will show evidence for diverse deformations in fine-grained lacustrine alternating with coarse-grained delta and fan. When we begun the work in Nahal Darga fan in early 1990s, this type of information on paleoseismicity, tectonic deformation, and lake level reconstruction was yet untapped in Israel. Then, and for several years, the sedimentary sequence of the Nahal Darga fan-delta was the best exposed in the Dead Sea area (and probably far beyond) as a very large flood in early January 1992 cleared the deeply incised banks to produce a remarkable natural trench walls (Fig. 2). From many aspects this fan delta is still a source of new data as incision continues to expose deeper sections with Dead Sea level continuing to drop at ~1 m/yr. Stratigraphically, the Darga's is the best-documented fan-delta in this tectonically active basin (Kadan, 1997; Enzel et al., 2000; Eyal et al., 2002). We specifically aimed at the detailed stratigraphy and age of the deformed beds within the Holocene fan-delta of Nahal Darga but also to understand the sedimentology that later served other researchers in the basin, especially those interested in lake level reconstructions. We stress that the exposure is still better than can be achieved through trenching.
We conducted two complimentary studies here: the subsurface and the exposures.

Shallow High-Resolution Seismic Study

High-resolution seismic profiles were acquired for the shallow subsurface in the Nahal Darga fan-delta (Figs. 3 and 4). Profiles 1, 2, and 3 are along the southern bank, the stream channel, and the northern bank, respectively and Profile 4 actuates as it follows the Dead Sea shoreline in 1996. The methods used can be found in Eyal et al, 2002 and in references therein. The lines below of high-resolution seismic lines intrude east into the northern Dead Sea basin on land and are connected well to the exposed stratigraphy.

We present here only the results of the reflection wave profiles, although exact determination of fault location within the profile is also based on diffraction waves. Usually the detection of faults on seismic sections is solved by visual interpretation of stacked sections. However, when detecting faults with a vertical displacement of less than the wavelength, a more sophisticated method must be used. To obtain reliable information about possible structural/ lithological discontinuities from seismic data, a procedure utilizing certain features known to be associated with the presence of such discontinuities is desirable. One such specific feature demonstrating the presence of faults on a seismic section is associated with the presence of diffracted waves in the vicinity of the discontinuity location. These waves can serve as a good indicator for fault detection. We extracted diffractions from the unmigrated stacked sections and used this information for identifying real discontinuities in the subsurface. The seismic interpretation is based on the presence of reflection horizons which, most probably but not necessarily, imply stratigraphic correlation. The time is given in seconds by Two Way Time (TWT). Based on a priori information (see details in Eyal et al., 2002) average velocity in the investigated area is about 2000–2500 m/s, so the maximal information depth achieved by these seismic profiles is about 400 m.

Profile 1 is obviously disturbed in its central part due to its proximity to the steep southern wall of the stream channel. Nevertheless, in its western part the bedding dips gently eastward and one normal fault can be interpreted. This fault is located underneath the exposed eastern part of the western deformation zone (see Fig. 5 at about 50 and 100 m at the northern and southern walls, respectively). At the eastern part of this profile (S.P. 137–150) two normal faults are defined below the area in which the large-scale deformations are exposed at the surface (see below).

Profile 2 was measured in the middle of the Nahal Darga channel and, therefore, can be related to both channel walls. The western termination of this seismic line lies approximately at the eastern part of the western deformation zone. No overlap exists between these two because an cement in the road prevented installation of the geophysical equipment further to the west. Therefore, the faults of the western deformation zone could not be detected in this seismic profile. The subsurface bedding dips gently toward the east as expected of eastward draining delta. An overall subsurface positive flower structure, comprised of a major reverse fault associated with a cluster of minor normal faults and a gentle fold, is evident. The location of these subsurface faults is below the area of the large scale deformations and the deformed blocks in the northern wall. At S.P. 140 a normal fault is observed in the subsurface extending almost to the surface. This fault is located east of the eastern deformation zone and underneath the surface area in which the bedding and cross-bedding become steep. Development of steeply dipping cross sets is commonly associated with deposition in deep water and, therefore, the existence of deep-seated normal faults beneath these sets may suggest deepening of the basin near the coast due to down faulting. It should be mentioned that earlier studies (e.g., Neev and Emery, 1967) used the steep bathymetry of the delta (yes, all the area you were waling on were under water 45 years ago) as indicator of the location of the fault. At S.P. 65–80 and 0.06–0.1 s (TWT) a

concave unconformity, probably the trace of an old small channel is observed. This is similar to small erosional channels exposed today or to the surface slumps.

Profile 3 is characterized by intensive normal faulting, which at S.P. 45–80 forms a flower structure pattern with a gentle fold between the secondary faults at S.P. 80, 0.1 s TWT. The main subsurface fault, at S.P. 50, overlaps the intensively faulted area of the western deformation zone along the northern channel wall. Actually, this subsurface fault is found along the continuation of a surface fault that exhibits the largest observed vertical displacement in this fan-delta. At the eastern part of the profile a large reverse fault (its upper part at S.P. 138, and lower at 157), which forms the western boundary of a gentle anticline (its hinge at S.P. 160 and 0.07 s TWT) is observed. This reverse fault is located just underneath the eastern deformation zone in the northern bank of the channel (Fig 5). A 25m wide, bowl shaped unconformity is observed at S.P. 170 and 0.1 s (TWT) representing either an old buried channel or another large scale deformation.

Profile 4 was measured along the Dead Sea shoreline in 1996 and shows (a) flat bedding and a few normal faults its southern part (up to S.P. 70), (b) from S.P. 70–190 a pattern of a positive flower structure with many normal faults intensively deforming the strata and also a few reverse faults and folds, (c) S.P. 195–305 is characterized by continuous bedding gently dipping southeastward. At S.P. 255 and time 0.1 s (TWT) the strata are discontinuous and the bowl shape of the discontinuity is similar to the cross section of the exposed large scale deformations of the eastern deformation zone (e.g. Fig. 5) or an erosional channel. An unconformity, including stratigraphic reduction of the thickness between two markers is observed between S.P. 190–300 and time 0.1–0.12 s (TWT).

There is a general consistency between the structures around the intersection points of line 4 with lines 1, 2, and 3.

2. The Exposed Stratigraphy and Deformation

Fig. 5 shows the exposed stratigraphy in the southern and northern banks of the incised Nahal Darga as was documented in 1995-1996. It should be noted (a) the original mapping of the exposures was carried out in more details at sites needed for both paleoseismology and lake level fluctuations and delta sedimentology. (b) The current exposure is not were we documented over a decade ago: stream meandered and walls collapsed but what is more interesting incision deeper into section, provides additional information.

Faults

Most faults and visible displacements are associated with two deformation zones; only a few occur outside these two zones (Fig. 5- Northern Wall). The faults are normal, and striations on some of the fault planes suggest dip–slip displacements; on a few faults, a small component of left-lateral slip was observed. Dips of the faults cluster in two main trends, ESE and WNW (Fig. 6). The faults from the respective deformation zones differ mainly in vertical displacement, in our ability to identify a specific fault in both walls, and in evidence for multiple displacements.

The normal faults in the western zone (Figs. 7 and 8) reveal multiple events that intersect almost the entire exposed section. Vertical components of displacement along these faults range from a few centimeters to 2 m. Examination of individual faults and beds in Fig. 8 indicates progressively larger offsets of older units, which in turn indicate multiple displacements. Along some faults, three discrete displacements were observed, whereas along other faults only one or two events were identified. It is difficult to determine which of the displacements on one fault affected nearby faults. Please not that the most spectacular faults are west-block down faults with minor displacements whereas the largest vertical displacement is on less clear fault. The youngest deformation in this western zone we can detect, is revealed in the northern wall of Nahal Darga. Between meters 15 and 30 m (Fig. 5), faults reach the surface. The age of the last activity on these faults is <2225±50 yr B.P., which is the age of the youngest deposit stratigraphically beneath the youngest faulted units (Fig. 5, meter 250 and follow units into meter 30). This age of faulting is supported by the youngest possible age of the faulted beach gravel that underlies the surface at the fault line and gently climes west to ~370 m; the last time a lake level reached 370 m below sea level to deposit such gravel was before 4000 yr ago (Kadan, 1997; Ben-David Novak, 2004). The earlier displacements observed on these faults is 9600–7000 yr B.P. (not calibrated; see Enzel et al, 2000 for calibration of Darga ages).

The faults in the eastern deformation zone (meters 255–320, Fig. 5) are confined to three layers and most clearly appear in a sandy layer bearing ripple marks. The vertical displacements along these faults are small and do not exceed 10 cm; no evidence for multiple movements was identified. The age of this "faulting", according to dated displaced strata, is <2400 yr B.P. No field evidence directly connects these minor faults with other tectonic structures. However, they are spatially associated with what we termed "allochthonous tectonic slumps" (see Large-scale deformation section below) to avoid any clarity as we have ideas what are they but no solution-field discussions are welcomed). To examine the possibility that the exposed faults are expressions of shallow gravitational movement, we acquired the above four high-resolution seismic profiles (Kadan, 1997; Eyal et al., 2002). These profiles demonstrate that large deep-seated subsurface faults exist below the two relatively narrow deformation zones.

Deformed Beds and Paleoearthquakes

Another field discussion…

At least 11 horizontal beds revealing internal deformation were observed in the stratigraphic sequence. Table 2 in Enzel et al (2000) lists the stratigraphic units in which these beds are located, their estimated ages, and the detailed stratigraphy and the thickness of the deformed bed, and the morphology of the major deformation observed in the specific bed. Most beds are sandy and were deposited in a near-shore environment (Kadan, 1997) and you will see many exposures of them. A few beds contain more silt and/or clay and evidently were deposited in a less energetic setting (Kadan, 1997). Beds that contain silt and clay are deformed into 'convolute lamination' whereas the pure sand layers are deformed into 'ball and pillow' and "flame" and "dike" structures (Sims, 1975; Hempton and Dewey, 1983; Allen, 1984; Maltman, 1994). The "ball

and pillow" structures occur commonly in the section. Generally the deformed beds have: (a) horizontal and sub-horizontal layering, (b) a thin cover of sediments with thickness ranging from a few centimeters to a maximum of 0.5 m, (c) random (but also some orientated) direction of the internal folds and other soft-sediment deformational structures, and (d) field relations indicating that the deformation occurred when the sediments were at the surface or very near the ground surface.

Most of the beds overlying these structures are deformed only at their lower contact, if at all, even if they are composed of similar or identical material. Some of the deformed beds can be traced for more than 100 m and are even recognized on both sides of the channel. Other deformed beds are truncated; these are only a few tens of meters long and are found only on one side of the channel. In some beds, the internal deformation disappears laterally as the layer thins and deformation reappears when the layer returns to its more characteristic thickness. This may imply (but not much data was collected) that there is a critical thickness at which a layer is affected by, and thus records, an earthquake. The vertical spacing of the deformed beds in the stratigraphic section is uneven. The proximity of these deformed layers may imply a

Large-Scale Deformations

The next section was written 10 years ago. Purposely I leave it unchanged.

In both walls of the channel, in the same stratigraphic position, there is an intensively deformed zone several meters thick (meters 260–320 in Fig. 2A and meters 280–350 in Fig. 2B). This zone is characterized by deformation of alluvial gravel, near-shore sands with ripple marks, and laminated lacustrine clays and silts with occasional aragonites. Each of these large scale deformations is composed of a zone of beds that are intensively deformed including vertical and overturned beds and folds. They exist at the same stratigraphic position in both walls, with no deformed beds above or below. When occasional floods erode the gravel that covers the floor of the 1996-7 channel, these large-scale deformations are also exposed in the stream bed between the two exposures at the walls. The slumps in these exposures are probably along a fault trending subparallel to the trace of the Jericho fault. Analysis of the high resolution seismic profiles (Eyal et al., 1997; 2002; see below) indicates that this elongated deformation is situated directly above a deeply seated flower structure that almost reaches the surface. We then were not sure about the origin of this large, stratigraphically well defined, linear zone of large-scale, soft-sediment deformation. We hypothesized that it is related to seismic activity along the Jericho fault located directly beneath it (Fig. 1). We suggested that if our hypothesis is correct, these slumps represent another style of deformation caused by a medium to large earthquake that affects fan-delta, perhaps saturated, deposits. Perhaps such slumping represents a larger earthquake than the earthquakes that caused liquefaction. The stratigraphy and radiocarbon ages help in narrowing the age range of this large deformation. The deformed beds within the slumps are bounded at their base by a bed dated at 2400 yr B.P. A piece of wood from the undulating plane that marks the base of the slump has an age of 2115±50 yr B.P. Two radiocarbon ages posdating the

deformation are 1440±110 and 1315±90 yr B.P. Stratigraphically, the deformation is also older than 1500 yr B.P., which is the age of the unconformity that truncates sediments that were deposited above the deformed material (Kadan, 1997). Therefore, the slump occurred sometime between 2400 and 1500 yr B.P., and probably after 2100 yr B.P.

Figure 9 shows the two situations; at the lower photograph you can see the 1999 first exposure of the large-scale deformation in the channel. Last year after incision but also stream self cleaning a new exposure shows that as the geophysics suggested and many hand dug holes did not, under the eastern deformation zone there is a fault and all the deformations on top of it could have been soft deformation responses to tectonic activity below. Some suggest that these deformations are sinkholes. We agree that two or three of them (will be shown in the field) resemble sinkholes but most not. These deformations have pushed up depositional units.

References

Allen, J. R. L. (1984). Sedimentary structures, their character and physical basis. *In* "Developments in Sedimentology **30,**" Vol. II, Elsevier, Amsterdam.

Bartov, Y., Bookman, R., and Enzel, Y., (2006). Current depositional environments at the Dead Sea margins as indicators of its past levels. In: Enzel, Y. Agnon, and M. Stein, (eds.)., New Frontiers in Dead Sea Paleoenvironmental Research. Geological Society of America Special Paper 401, p. 127-140.

Ben David-Novak, H., Morin, E., and Enzel, Y., (2004). Modern extreme storms and the rainfall thresholds for initiating debris flows on the hyperarid western escarpment of the Dead Sea, Israel. Geological Society of America Bulletin. v. 116 (5-6): 718-728

Bowman, D. (1974). "River Terraces in the Dead Sea Area—Morphological Aspects." Unpublished Ph.D. dissertation, Hebrew University of Jerusalem (in Hebrew with English Abstract).

Dunne, L. E., and Hempton, M. R. (1984). Deltaic sedimentation in the Lake Hazar pull-apart basin, sout-eastern Turkey. *Sedimentology* **31,** 401–412.

Enzel, Y., Kadan, G., and Eyal, Y. (2000). Holocene Earthquakes in the Dead Sea Graben from a Fan-Delta Sequence, Quaternary Research, 53, 34–48,.

Eyal, Y., Bruner, I., Kadan, G., Enzel, Y., and Landa, E. (1997). "Association of Surface and Subsurface Tectonic Structures at the Holocene Fan-Delta of Nahal Darga, Dead Sea Israel." Holon, Israel. The Geophysical Institute of Israel Report No. 704/150/96.

Eyal, Y., Brunner, I., Kadan, G., Enzel, Y., and Landa, E. (2002). High-resolution seismic study of the Nahal Darga fan-delta, Dead Sea, Israel, with the aim to relate the surface and subsurface tectonic structures. European Geophysical Union Stephan Mueller Special Publication Series, 2, p. 21-33.

Kadan, G. (1997). Evidence for Dead Sea Lake-Level Fluctuations and Recent Tectonism from the Holocene Fan-Delta of Nahal Darga, Israel, Unpublished M.Sc. thesis, Ben Gurion University of the Negev (in Hebrew with English Abstract).

Maltman, A. (1994). "The Geological Deformation of Sediments." Chapman & Hall, London/New York.

Manspeizer, W. (1985). The Dead Sea Rift: Impact of climate and tectonism on Pleistocene and Holocene sediments. *In* "Strike-Slip Deformation, Basin Formation and Sedimentation" (K. T. Biddle and N. Christie-Black, Eds.). *Society for Economic Paleontology and Mineralogy Special Publication* **37,** 143–158.

Neev, D., and Emery, K. O. (1967). The Dead Sea, depositional processes and environments of evaporites. *Geological Survey of Israel Bulletin* **41.**

Niemi, T., and Ben Avraham, Z. 1994. Evidence for Jericho earthquakes from slumped sediments of the Jordan river delta in the Dead Sea. Geology, v.22, 395-398

Shapira, A., Avni, R., and Nur, A. (1993). A new estimate for the epicenter of the Jericho earthquake of 11 July 1927. *Israel Journal of Earth Sciences* **42,** 93–96

Sims, J. D. (1975). Determining earthquake recurrence intervals from deformational sructures in young lacustrine sediments. *Tectonophysics* **29,** 141–152.

Sneh, A. (1979). Late Pleistocene fan deltas along the Dead Sea rift. *Journal of Sedimentary Petrology* **49,** 541–552.

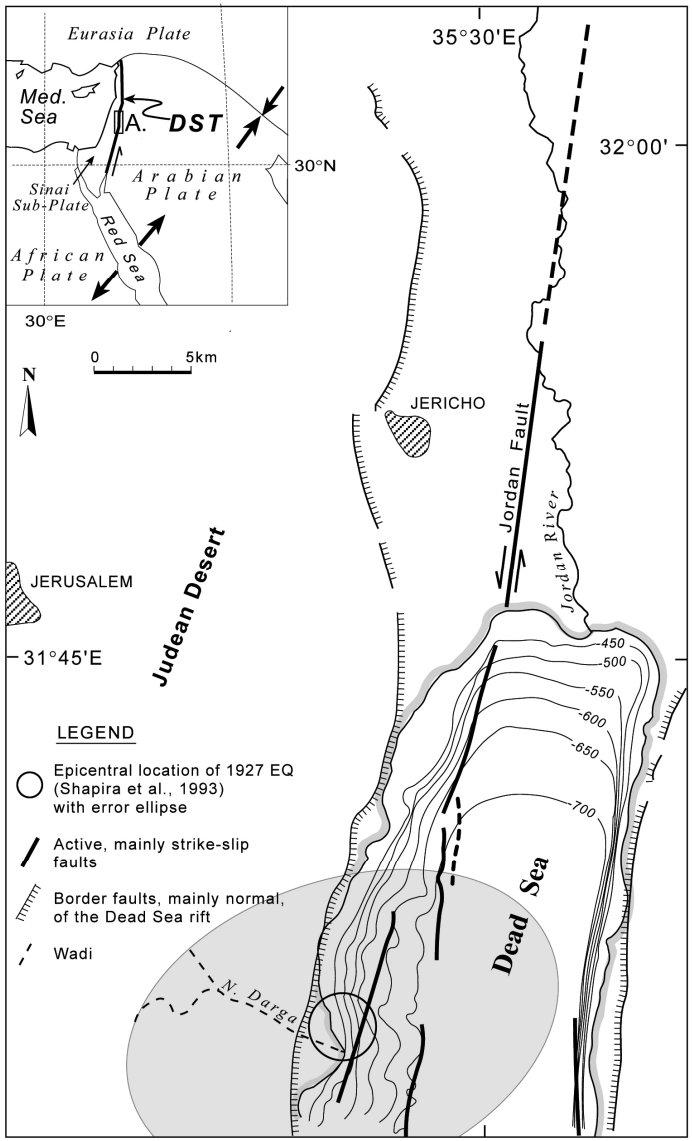

Figure 1: General location map and the general tectonic setting of the northern part of the Dead Sea (after Niemi and Ben-Avraham, 1994). The epicenter location of the Jericho 1927 earthquake (Shapira et al., 1993) is about 2 km northeastward of the Nahal Darga fan-delta. The contour lines are the bathymetric contours of the Dead Sea.

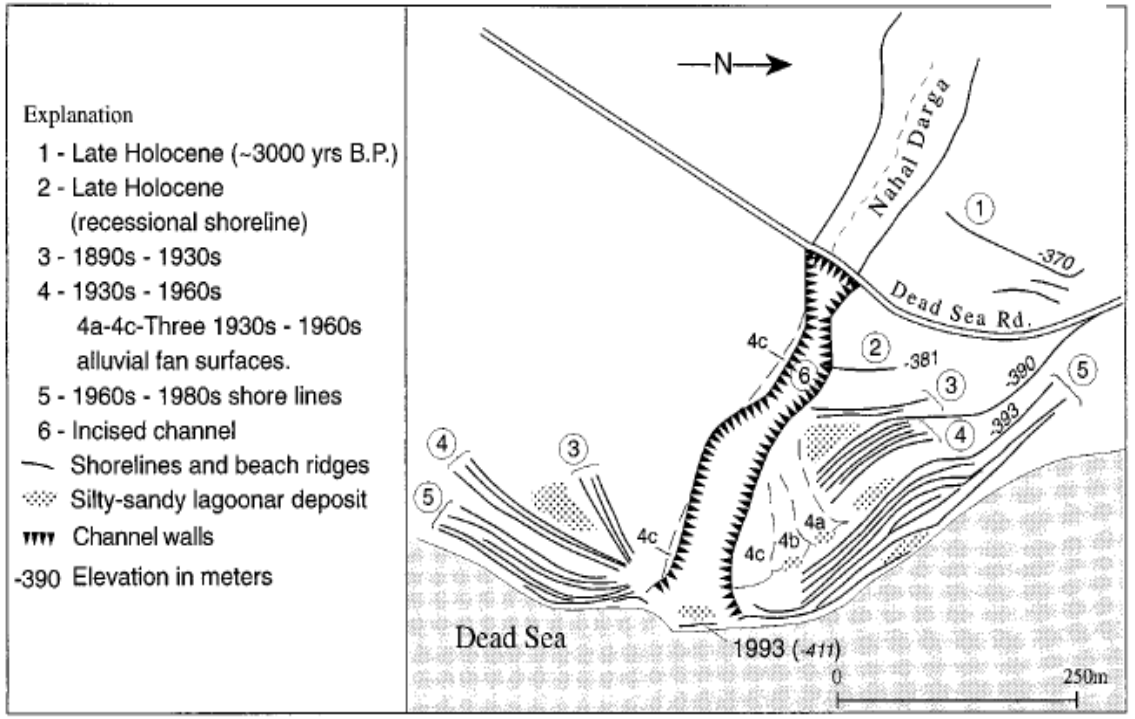

Figure 2: Shorelines of the Dead Sea on late Holocene fan-delta surfaces of Nahal Darga. (from Enzel et al., 2000).

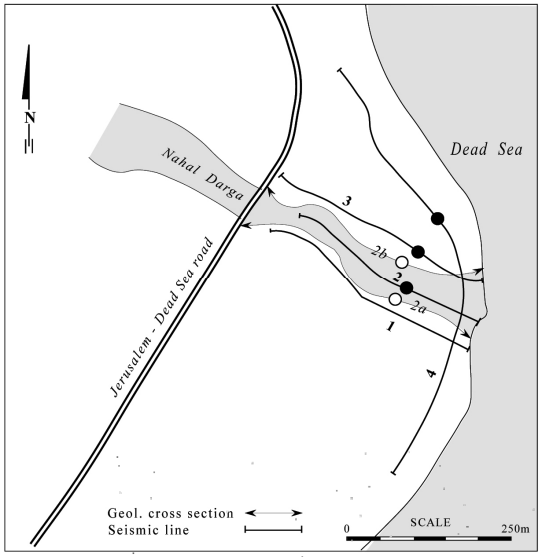

Figure 3: The outline of the seismic profiles lines 1 to 4 . 2a and 2b are the southern and the northern geologic cross section exposed along the channel walls. The open circles mark the center of the location of the exposed heavily deformed sediments (in 1997). The solid circles on the seismic profiles represent the first appearance, from west, of the large subsurface reverse faults and flower structures, probably representing the western boundary of the eastern deformation zone (S.P. 100, 140 and 190 in profiles 2, and 3, and 4, respectively).

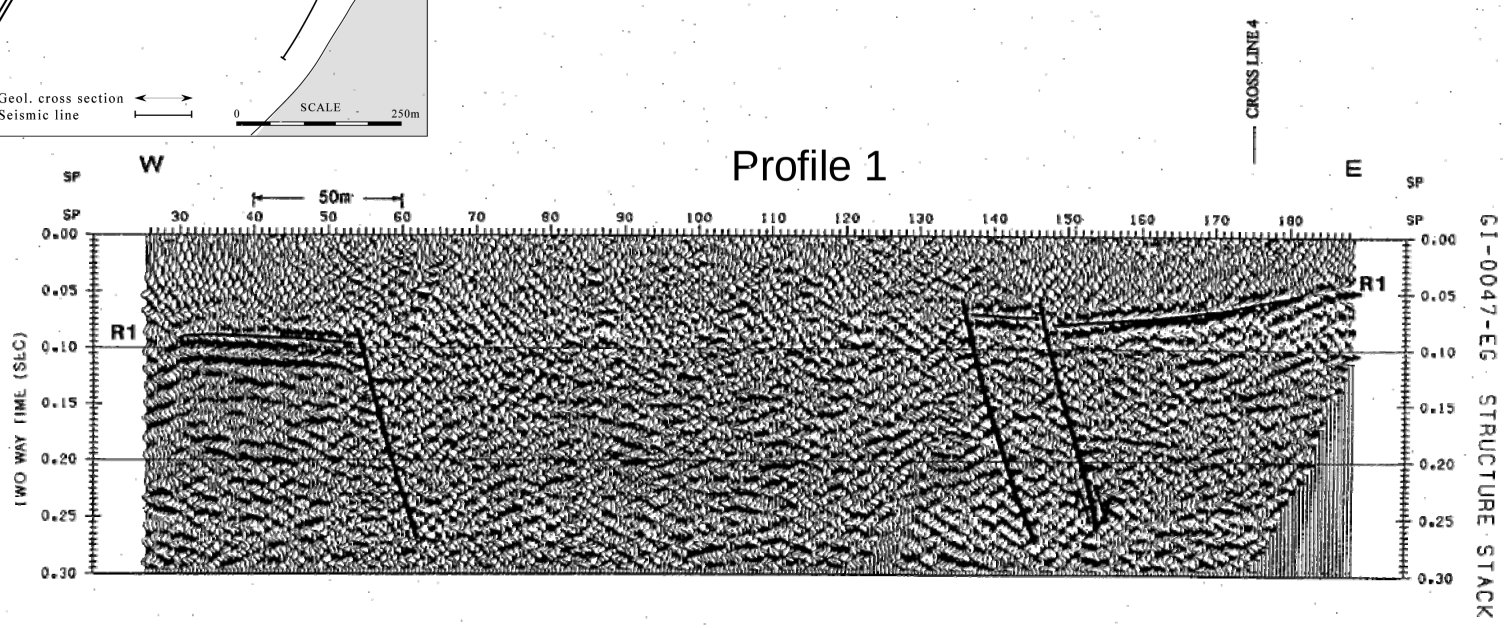

Figure 4: Interpreted multichannel high-resolution seismic profiles from the Nahal Darga fan-delta. The locations of these profiles are shown in Fig. 3. The interpreted seismic markers do not have any stratigraphic correlation. The exact determination of fault location within the profile is also based on diffraction waves. The time is given in seconds by Two Way Time (TWT). The vertical lines above the seismic profiles in each of the profiles relate to the crossing location of seismic profiles. For example, the vertical line at the eastern part of profile 1 is the location where profile 4 crosses profile 1. The three vertical lines above profile 4 are the locations where, from left to right, profiles 3, 2 and 1 cross profile 1 respectively.

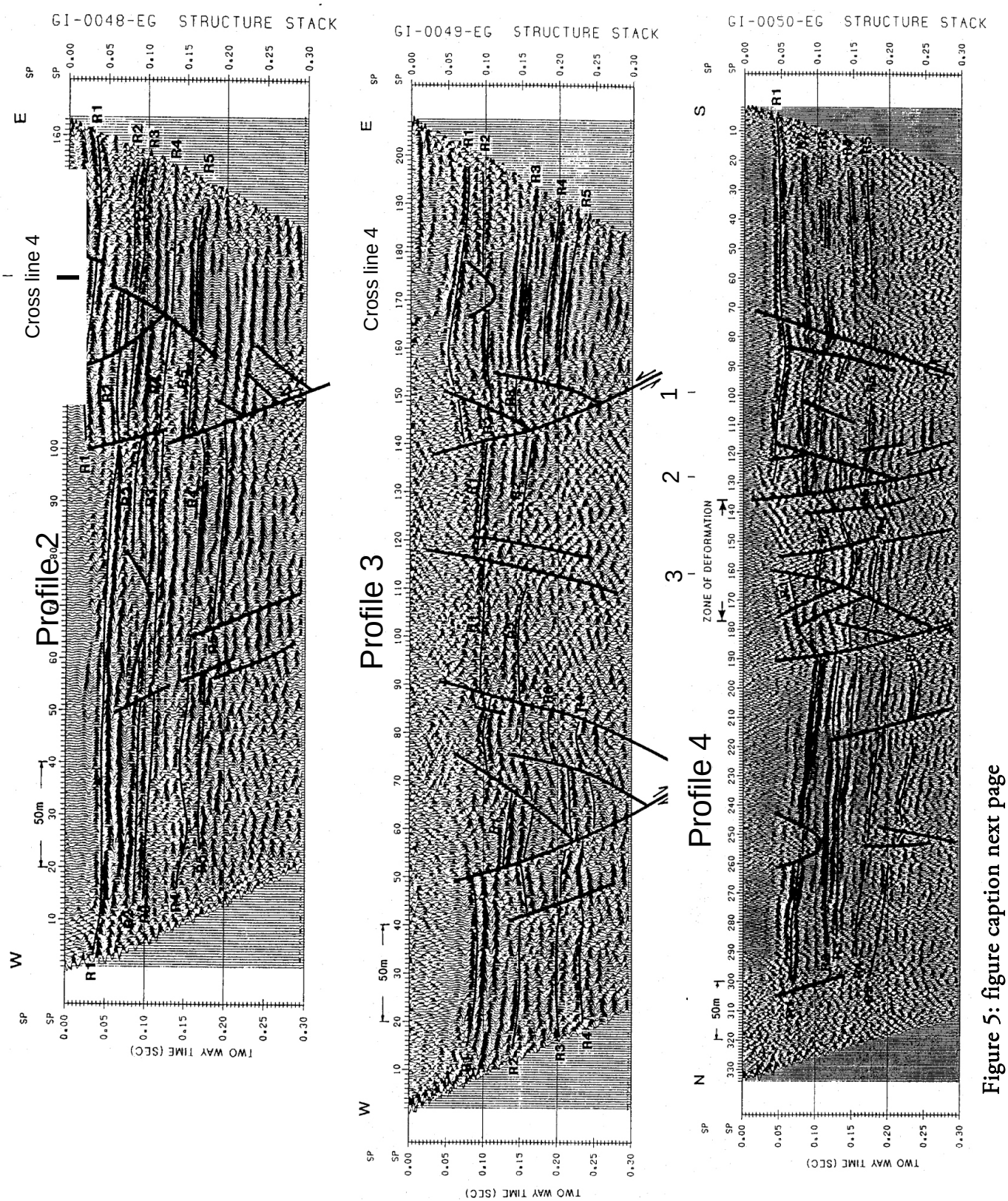

Figure 5: figure caption next page

Figure 5:
The stratigraphy of the southern wall and the northern wall of the incised channel (Fig. 1) of Nahal Darga in 1996. No vertical exaggeration. The scale at the base of each section is in meters along the base of the section and therefore it somewat longer from the shortest distance from highway to shore. The left end of each of the five sections is connected to the right end of the section below. Numbers in circles are easily identified field stratigraphic units; each may contain a few to many beds and more than one lithology. The main lithology is marked. See Table 1 in Enzel et al.(2000) for details and calibration of these ^{14}C BP ages. Lithologies: 1, fluvial gravel; 2, near-shore sand with frequent ripple marks; 3, well-bedded to laminated clay silt with occasional aragonite; 4, well-to medium sorted coarse sand, pebbles and cobbles in sets of the delta front; 5, well-sorted prograding beach deposits with lenses of clay–silt lagoonal deposits; 6, the major unconformity in the section; its age is roughly estimated at approximately 4000 yr B.P. (Kadan, 1997).

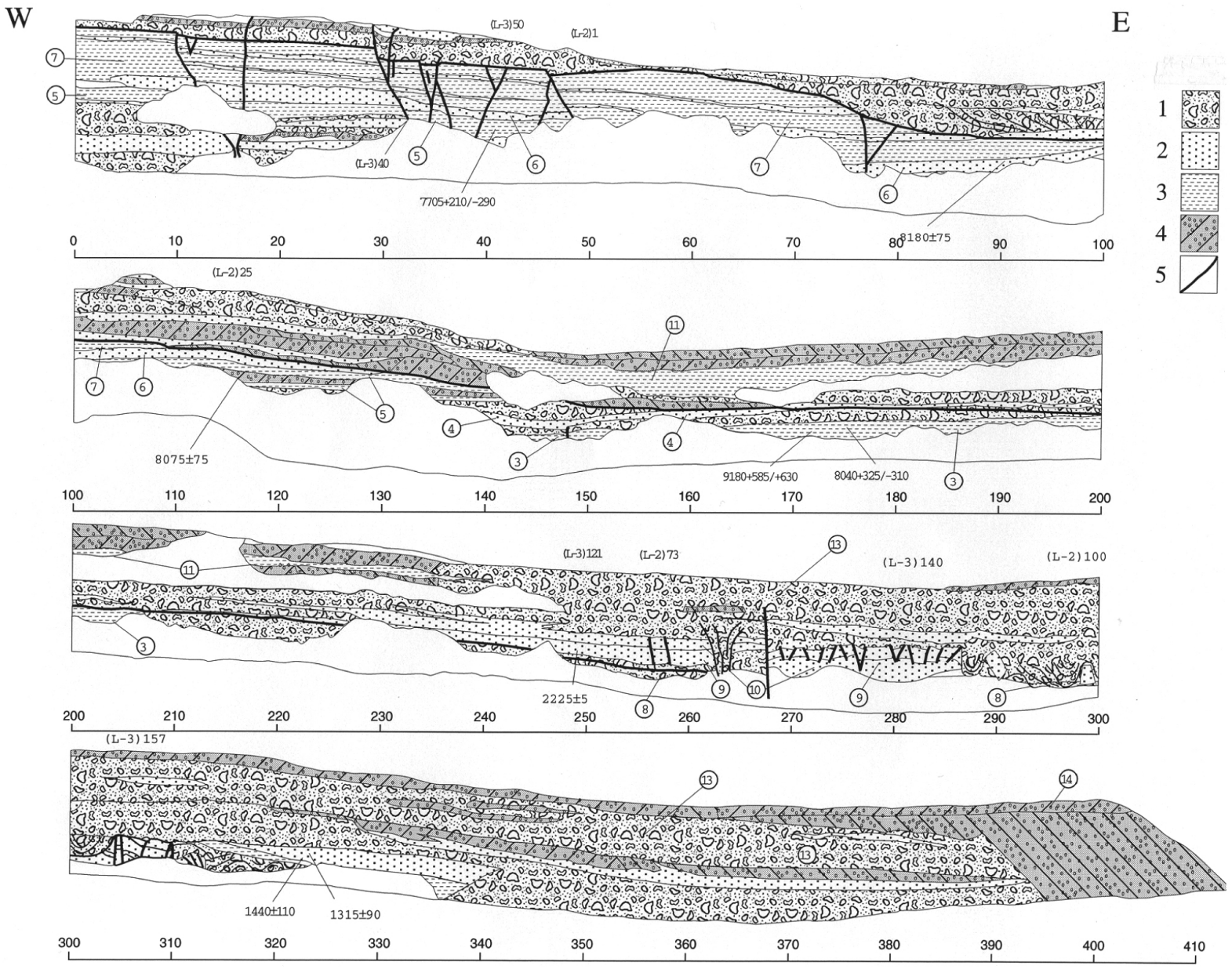

Figure 5: Southern wall in 1996

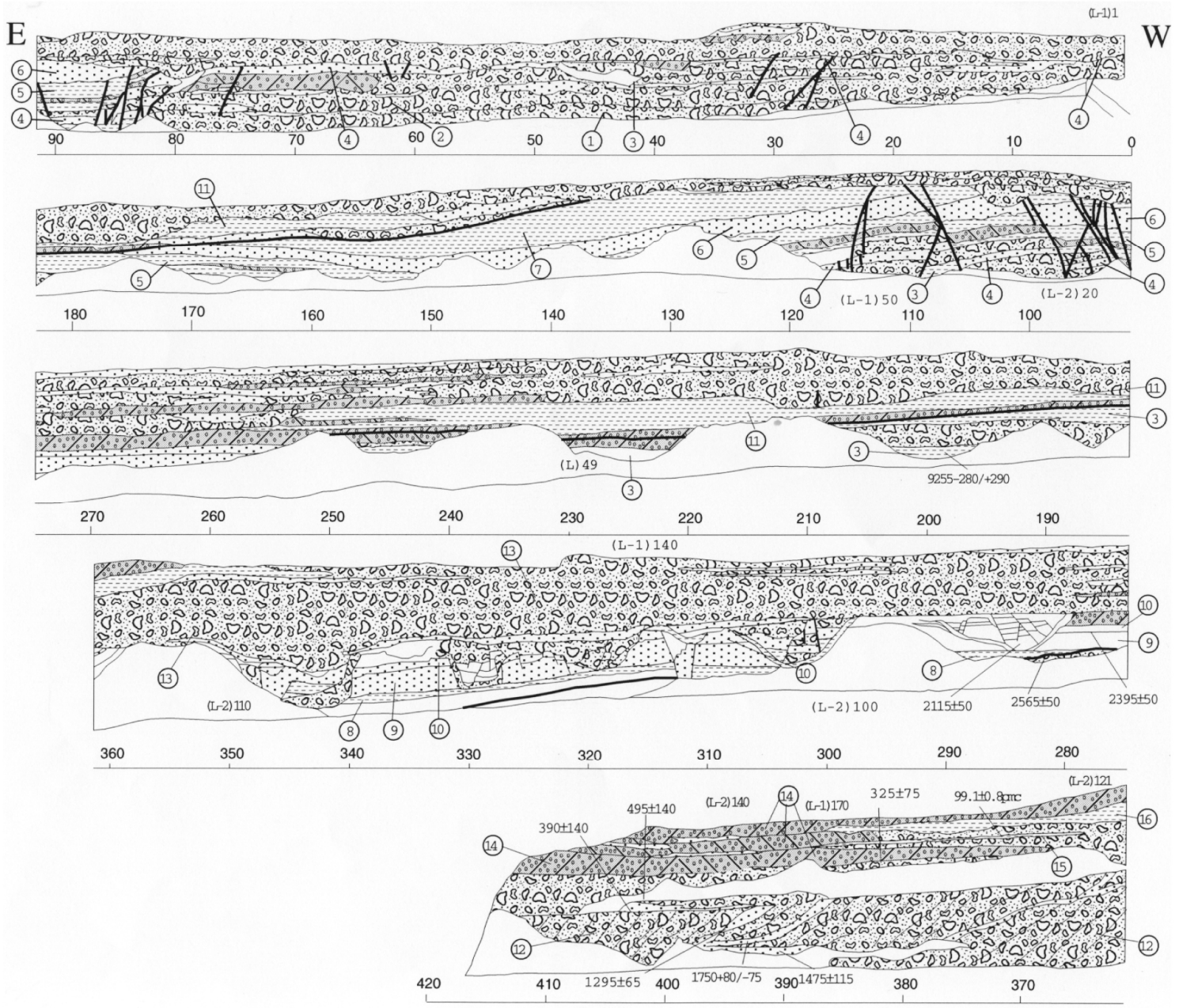

Figure 5: Northern wall

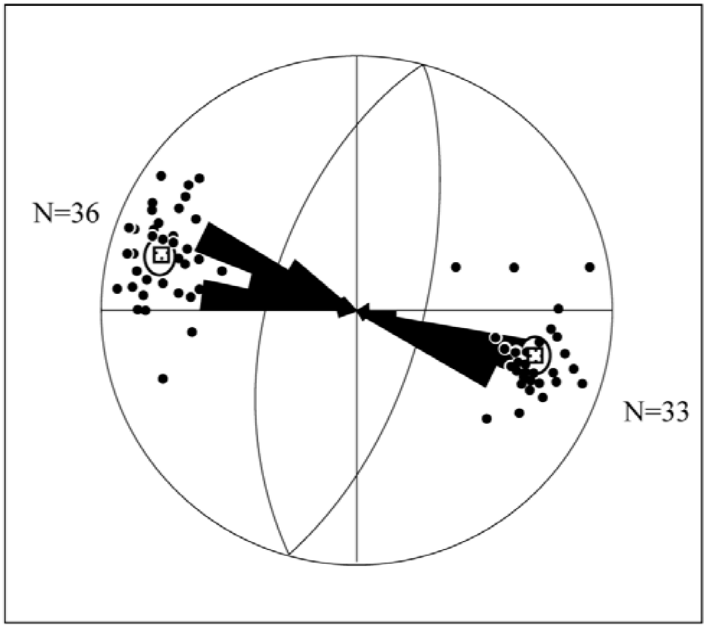

Figure 6: Stereographic projection, lower hemisphere, of 99 poles (dots) to fault planes from Nahal Darga. The great circles are the mean fault planes of the two groups of faults striking NNE-SSW with dips to WNW and ESE. The small circles outline the 95 range.

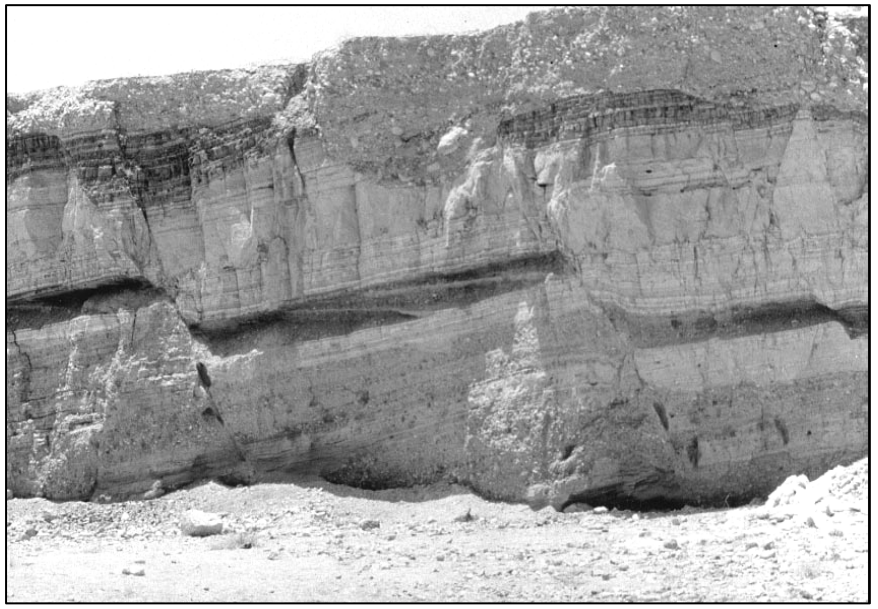

Figure 7: A photograph showing faults A and B of Figure 8 exposed at the southern wall. See Figure 4 for scale and explanations. Note the tilted lacustrine and fluvial deposits with well-pronounced prograding beach ridge deposits in the middle of the section. The erosional channel parallels the faults and was filled with coarse sandy gravel of unknown age and was truncated and covered again by a very thin (0.5 m) 1960s alluvial-fan deposits.

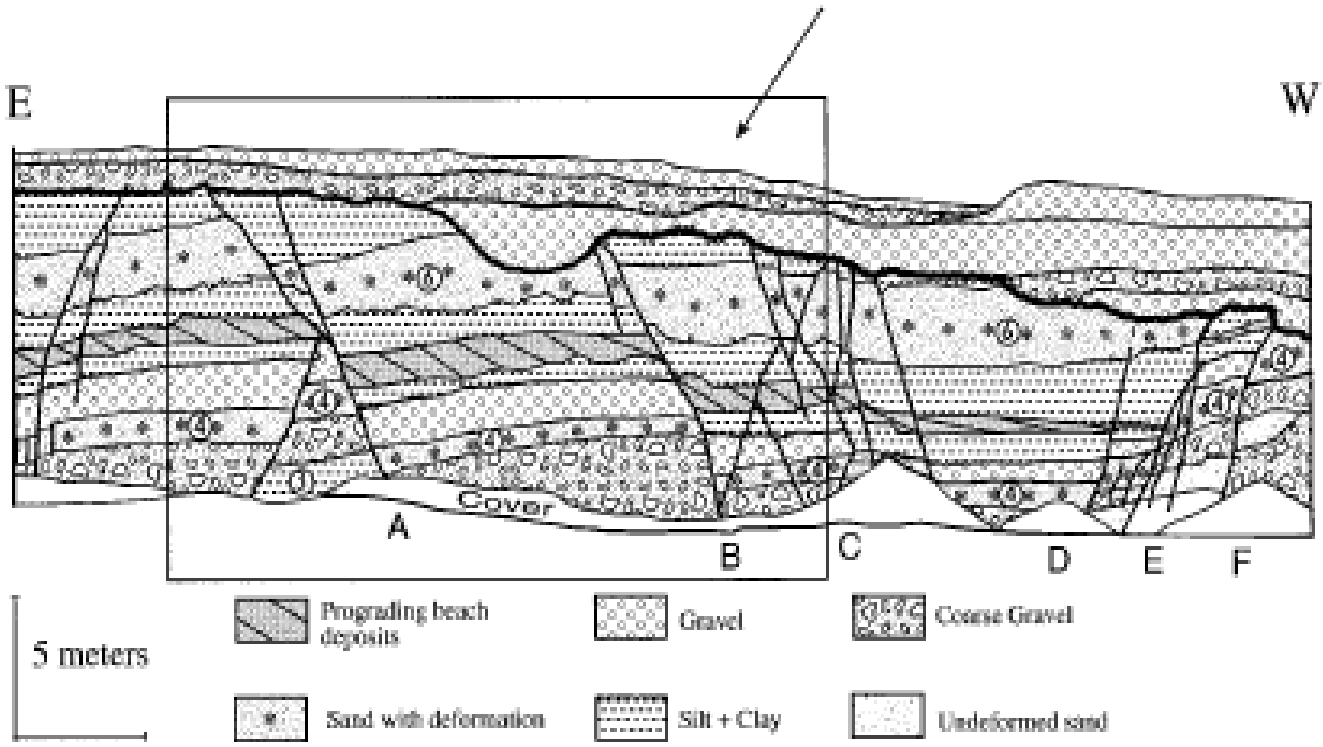

Figure 8: Detailed map of the western faulted zone at the southern wall of Nahal Darga. They were probably experienced three distinct displacements. Total vertical displacement of unit 4 on faults D–F is approximately 4.5 m. When displacement is measured from the two ends of the figure and unit thickness changes are accounted for, the total displacement is 3.5 m. The prograding beach deposits are displaced approximately 3.5 m by faults D–F but with lower total displacement in the entire zone. The units underneath the erosional unconformity (marked as a dark solid line) are 7000 yr B.P. Most of these units grade into sand a few tens of meters to the east. The age of the erosional channel and its associated deposits directly above the unconformity is not clear. The age of the unconformity itself is probably 4000 yr B.P. (Kadan, 1997). The top gravel unit is a historical alluvial-fan, which was active since the early 1900s but here we think it is of the late 1960s. Only minor fractures without any observed displacement cross the unconformity; none reach the surface.
When in the field and visit this exposure, it is time to turn around and watch the northern wall.

Figure 9:

November 2007 photograph during documentation of the exposed fault and deformations following 4+ meters of incision of channel bed

Photograph in 1998

Large scale deformation exposed in channel bed after a flood, in-between the deformation in the two walls

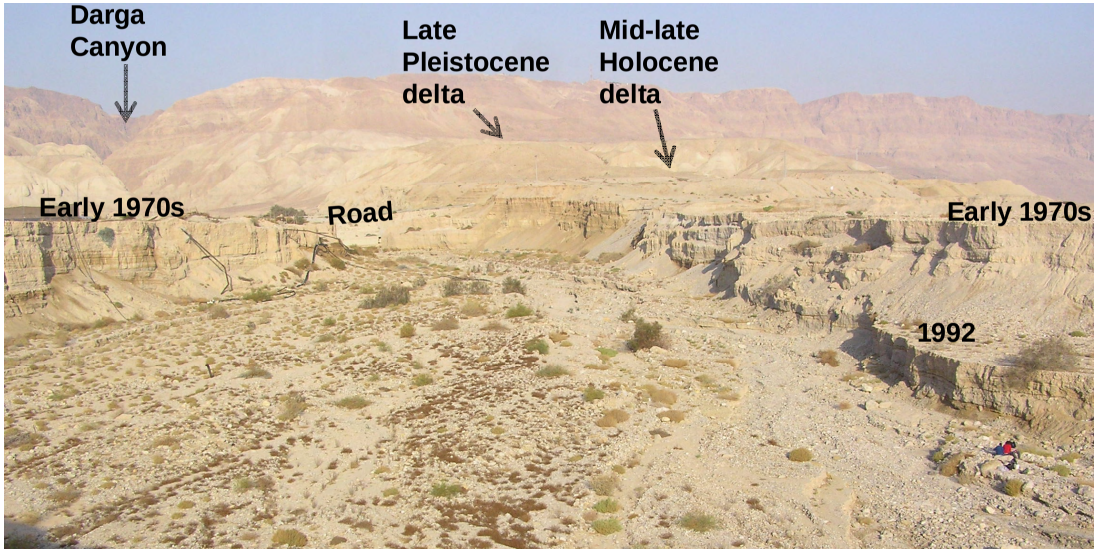

Figure 10A: Nahal Darga, view to the west\upstream in 2007. Note the deep incision since the late 1960s and the early 1970s. The channel is maintained in because of the artificial cement knickpoint at the road (see Ben Moshe et al., 2008, *Geomorphology*). During our Mid-1990s work the channel bed was at about the level of the 1992 terrace.

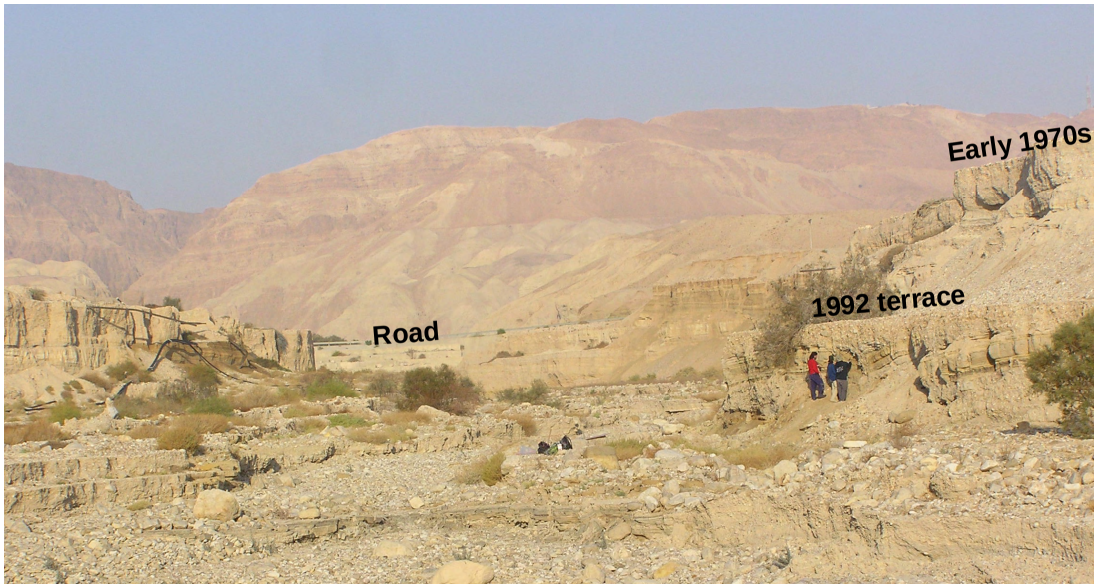

Figure 10B : Nahal Darga, view to the west\upstream in 2007. The students stand next to a new exposure.

Collapse-sinkholes near Mineral Beach - Do sinkhole clusters reveal active faults buried within the sediments of the Dead Sea basin?

Meir Abelson[1*], Gidon Baer[1], Yoseph Yechieli[1], Eyal Shalev[1], Vladimir Shtivelman[2]

[1]Geological Survey of Israel

[2]Geophysical Institute of Israel

meira@gsi.gov.il

* Field guide

Since the early 1980s, more than 2000 sinkholes have developed along the western coast of the Dead Sea (DS). All sinkholes are concentrated within a narrow strip with a width of tens meters to <1 km (Figs. 1-2). More than 75% of the sinkholes occurred in the last decade, in a rate of 150-300 sinkholes per year (Fig. 3). This highly dynamic phenomenon occurs due to dissolution of a salt layer buried between 20 – 70 m (depth to layer top), which in turn forms cavities causing the collapse of the overlying sediments (Fig. 4). The whole process is triggered by the rapid decline of the DS level and by eastward migration of its coastline. The eastward migration of the DS coastline is accompanied by the eastward migration of groundwater brine and intrusion of groundwater undersaturated with respect to halite. The undersaturated groundwater dissolves the salt layer, hence forming the underground cavities (Yechieli et al., 2006; Shalev et al., 2006).

Sinkhole lineaments along cryptic, likely active, young faults

The sinkholes around the DS cluster in more than 40 sites, where each site includes from 1 to more than 100 sinkholes. Almost all sinkhole clusters display a clear linear shape. Comparison between the trends of the sinkhole lineaments, the exposed faults, and the zigzagging rift wall segments shows a striking similarity (Fig. 5a and 5b). All features show a predominantly bimodal distribution with NE and NW principal directions (Fig. 5b). No relationships are found between sinkhole lineaments and other surface features such as ancient or current DS shorelines, or alluvial fans. These observations suggest that sinkhole formation is controlled by faults concealed within the rift fill.

To confirm this linkage between buried faults and sinkhole lines we conducted 10 profiles of seismic reflection across and along sinkhole lines in six different sites (Figs. 5-6). In the examined sites the sinkhole lineaments were found to overlie prominent discontinuities. For instance, profiles across the sinkhole lines in the Neve Zohar and Hever-south sites (Fig. 1) display clear discontinuities interrupting the reflectors beneath the sinkhole lines (Figs. 5c,d and 6) that offset young sediments several thousands of years old. In the Hever-south site layers shallower than 20 m are offset beneath the sinkhole line (Fig. 5d). ^{14}C dating of the salt layer at depth of 27 m (sampled from a borehole in this site) indicates 10 kyr (Fig. 5d), suggesting that the offset layers are younger than 7500 years. This implies that the faults are young and likely active, but bear no surface manifestation other than the sinkhole lineaments.

Radar interferometry, land subsidence, and young faults

Subtle land subsidence along the DS coast was recently detected by InSAR [*Baer et al.*, 2002]. Sixteen SAR scenes obtained by the European Remote Sensing satellites ERS-1 and ERS-2 during 1992 to 1999 were analyzed, spanning periods of 2 to 71 months. Gradual subsidence features, a few hundred meters to a few kilometers long, with subsidence rates of 0-20 mm/yr, were found in association with most sinkhole sites. This subsidence was attributed to the consolidation of the clayey (and/or silt) layers within the alluvial fill due to the drop in level of the DS and the associated drop of groundwater level [*Baer et al.*, 2002].

Sinkhole lines occur either within the subsiding areas, or along the boundaries of these areas (Fig. 7). For example, in the En-Gedi south area, a sinkhole line oriented 062° (Fig. 7) is located within the subsiding area sub-parallel to its straight northwestern boundary; the southwestward continuation of the sinkhole line coincides with another straight boundary further to the west (Fig. 7). This configuration is interpreted as two sub-parallel ENE trending faults, suggesting that both sinkhole lines and linear boundaries of the subsiding area reflect buried faults.

Role of faults and land subsidence in the formation of the DS sinkholes

The appearance of the fault-related sinkholes, combined with the linear boundaries of subsiding areas observed by InSAR, complement our view of the tectonic structure buried in the alluvial fill. In the En-Gedi area, for example, the InSAR and sinkhole lineaments suggest two sets of faults (Fig. 7). The strikes of one set are between 347°-360°, in agreement with the common direction of the rift-margin faults. This is also the most common trend of the sinkhole lines in the entire area. A zigzag pattern is formed by an additional, secondary group of lines oriented ~60°.

Considering all the observations mentioned above, we suggest a mechanism that combines gradual land subsidence with the formation of the DS sinkholes (Fig. 8). The trigger for both phenomena is the drop in the DS level and of the surrounding groundwater levels. This drop decreases the pore pressure in the aquifer system and increases the effective stresses in the rock column [*Terzaghi*, 1925; *Galloway et al.*, 1998; *Amelung et al.*, 1999]. Consequently, areas of higher clay content are differentially compacted [*Baer et al.*, 2002]. The decline of the DS level also leads to eastward migration of the saline-fresh water interface, bringing water under-saturated with respect to halite towards the buried salt layer, causing salt dissolution and formation of cavities. This notion is strongly supported by the finding of undersaturated water below and above the salt layer in boreholes near the sinkhole site of En-Gedi plantations (see Fig. 1 for location). Several-meter-thick aquiclude layers above and below the salt layer (as indicated in several boreholes [*Yechieli et al.*, 2006; *Abelson et al.*, 2006], Fig. 2d) may restrict access of the sub-saturated water to the salt layer. However, differential compaction could generate and localize shear strain within the clayey layers along or parallel to pre-existing faults. These faults may then serve as conduits for the sub-saturated water to percolate to the salt layer (Fig. 8b) and

promote the development of sinkholes (Abelson et al., 2003). The ascent of sub-saturated water is possible due to overpressure in the confined aquifers below the salt and clayey layers, which was found to be higher than the upper phreatic aquifer in the boreholes along the DS coast (*Yechieli et al.*, 2006). We therefore propose that sinkhole distribution and gradual land subsidence features are controlled by, and reflect the young and possibly active faults concealed within the fill of the DS basin. It appears that sinkhole lines and subsidence features can serve as a useful tool for mapping active faults in this seismically active region. We speculate that a strong earthquake may open these faults through the aquiclude layers which in turn may promote flow of undersaturated groundwater towards the salt layer, hence catalyzing sinkholes formation.

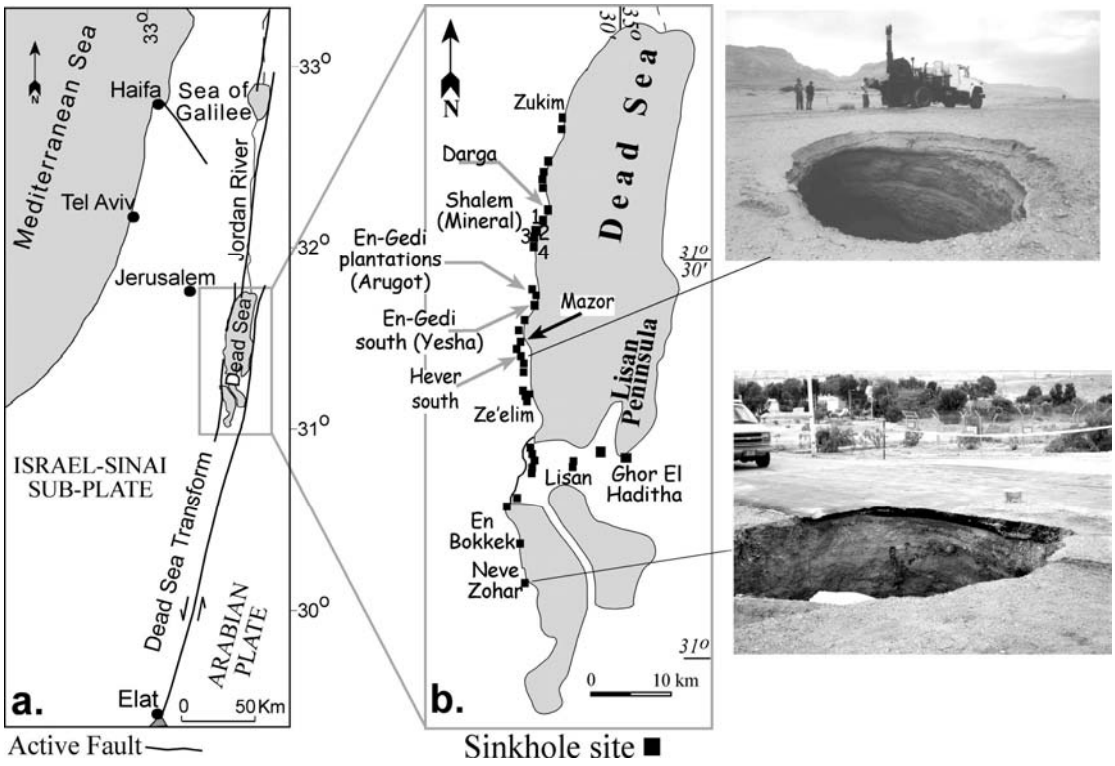

Figure 1: (a) Location map showing the Dead Sea pull-apart basin along the Dead Sea Transform. (b) Distribution of sinkhole sites along the Dead Sea coast and two examples of sinkholes.

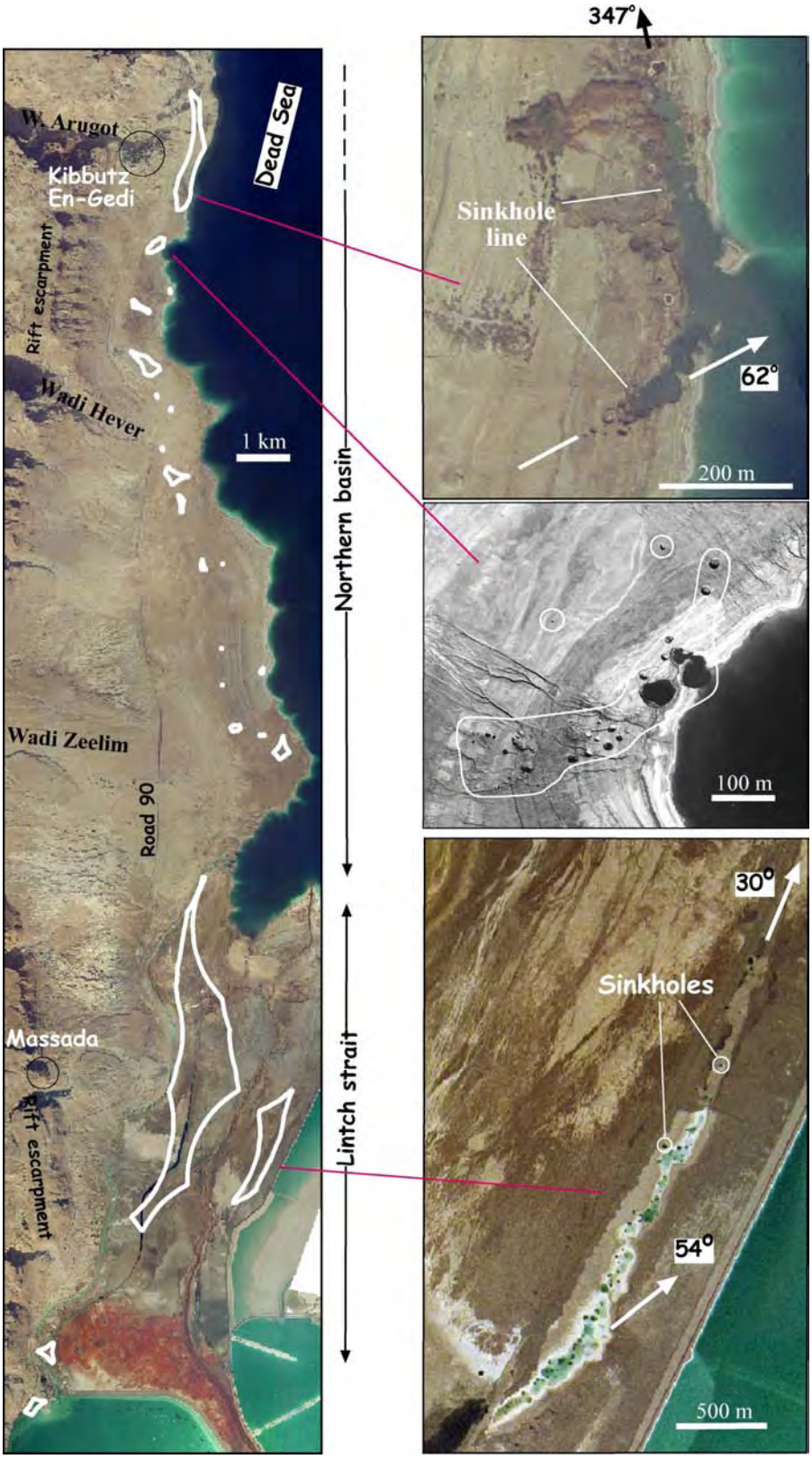

Figure 2. Rectified aerial photograph along the Dead Sea coast (a) between Lynch Strait and En-Gedi (see Fig. 1 for location) (Yechieli et al., 2006). White polygons denote sinkhole sites. Road 90 is the main road running through the Dead Sea rift valley. The figure displays the widest part, ~1 km, of the strip where more than 2000 sinkholes have developed since the early 1980s. Three aerial photographs show a closer view of three sinkhole sites (b-d). Note the preferred orientation of sinkhole clusters which follow concealed tectonic lineaments.

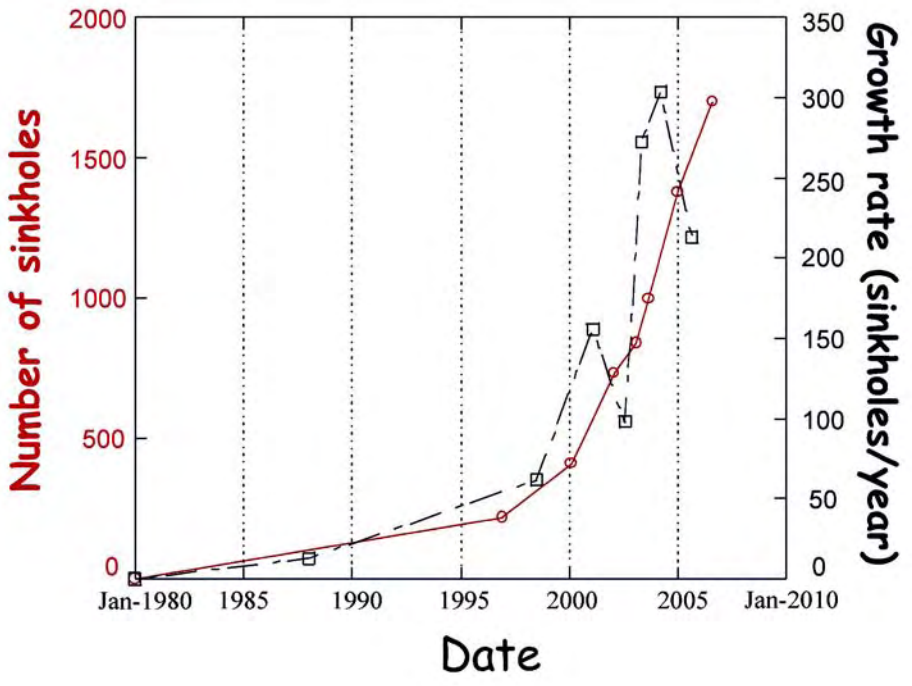

Figure 3: Rate of sinkholes growth since the early 1980s. Number of sinkholes (red) and growth rate (black) are presented versus the calendar year (Abelson et al., 2006).

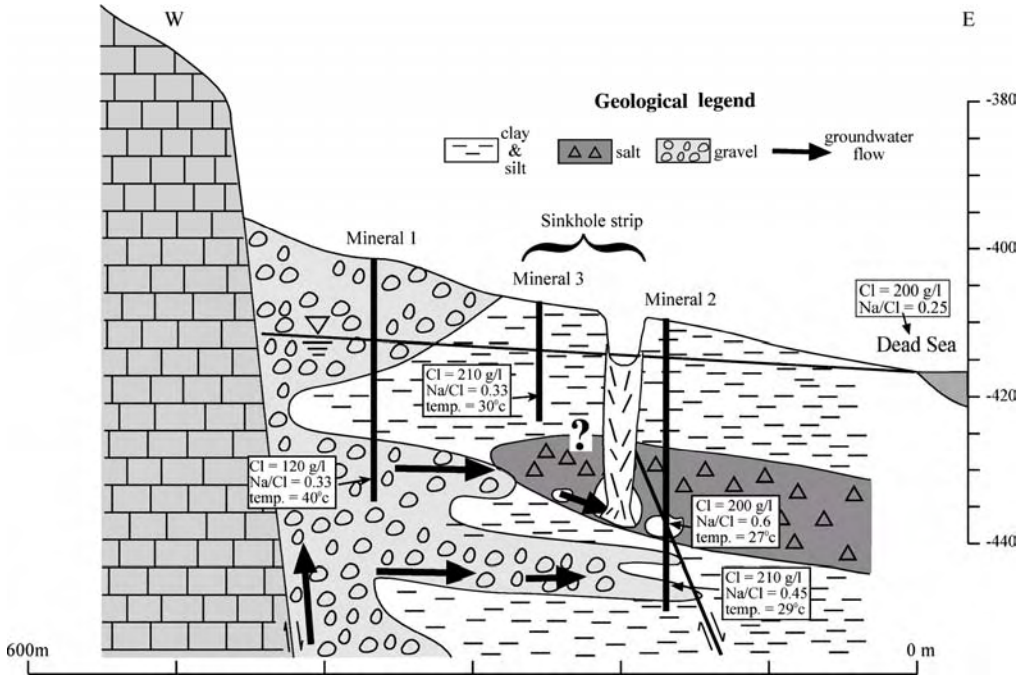

Figure 4: A hydrogeological schematic section across the elongated swarm of sinkholes in the Shalem-2 site (see Fig. 1 for location) (after Yechieli et al., 2006). The Mineral-2 borehole penetrated a cavity in the salt layer with water that exhibits a clear signal of salt dissolution (Na/Cl=0.6). Much less saline water (Cl=120 g/l, unsaturated with respect to halite) and also lower Na/Cl values (0.33) was found in the nearby Mineral-1 borehole. The sinkholes which develop along a lineament are found close to the western margin of the salt layer distribution.

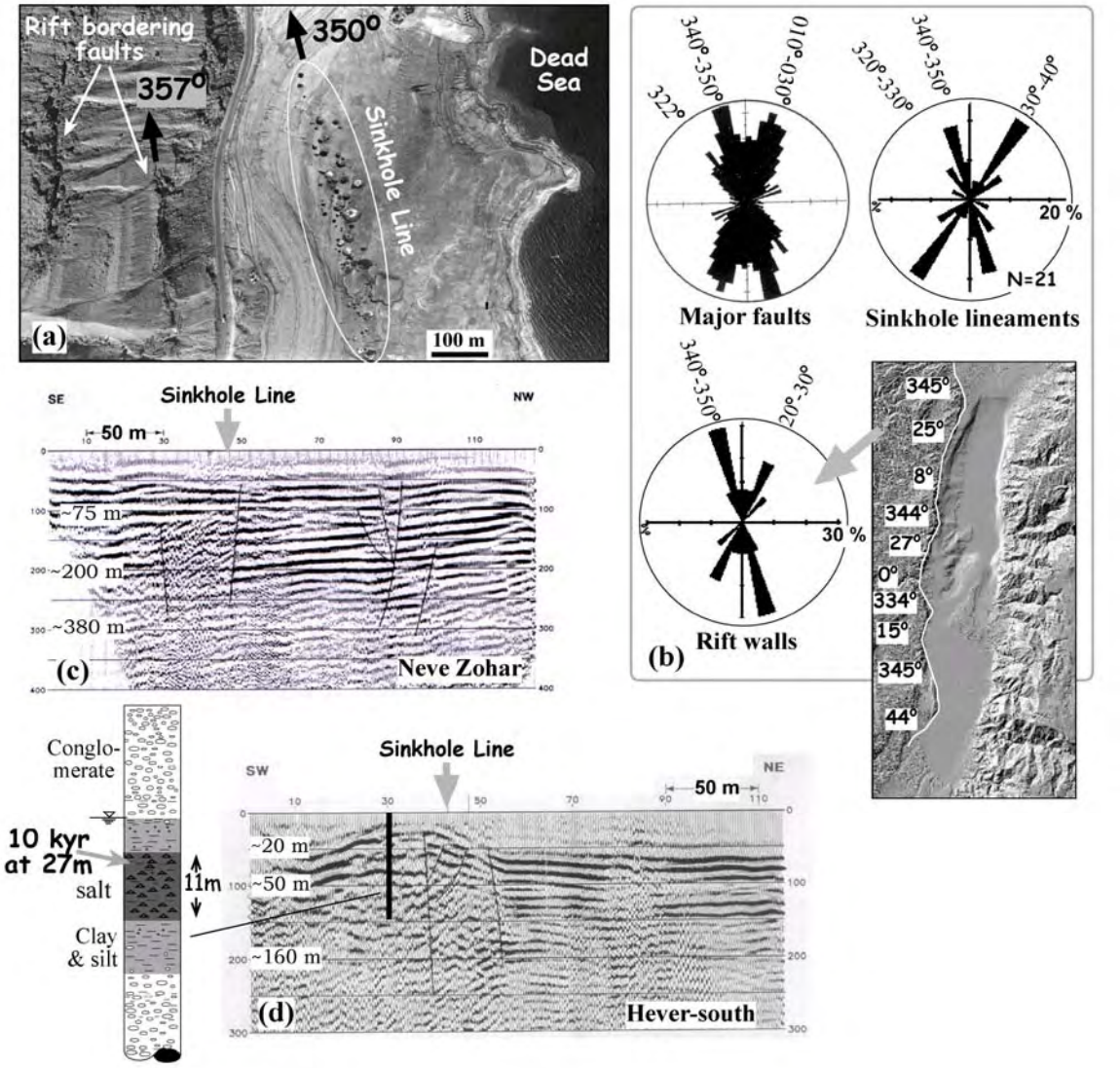

Figure 5: Sinkhole lineaments and buried faults (after Abelson et al., 2003). (a) A rectified air photograph from 1999 showing the sinkhole site of Hamme Shalem (Fig. 1). The sinkholes are aligned sub-parallel to the local rift-margin faults. (b) Area weighted, rose-diagrams of strikes of major faults on the western margin of the DS rift [*Sagy et al.*, 2002] (cumulative length 322 km), sinkhole lines, and strikes of the western rift wall segments displayed on a digital shaded-relief map [*Hall*, 1994]. Note the similar bimodal distribution of the various populations, implying a tectonic control on the sinkhole lines. (c) and (d) Seismic reflection profiles across the Neve Zohar and Hever-south sites (see Fig. 1 for location) showing prominent discontinuities beneath the sinkhole lines. In Neve Zohar (c), a sequence of disturbed layers is bounded by the two discontinuities interpreted as faults. The northwesterly discontinuity is beneath the sinkhole line. A seismic reflection profile parallel to the sinkhole line at this site shows no discontinuity, suggesting that the buried discontinuities/faults are parallel to the sinkhole line. A summary of borehole findings (80 m deep) from Hever-south site is presented in (d); ^{14}C dating from a 27m-deep clay horizon within the salt layer indicates age of 10,000 years, suggesting that the observed offsets shallower than 20 m are younger than 7500 years.

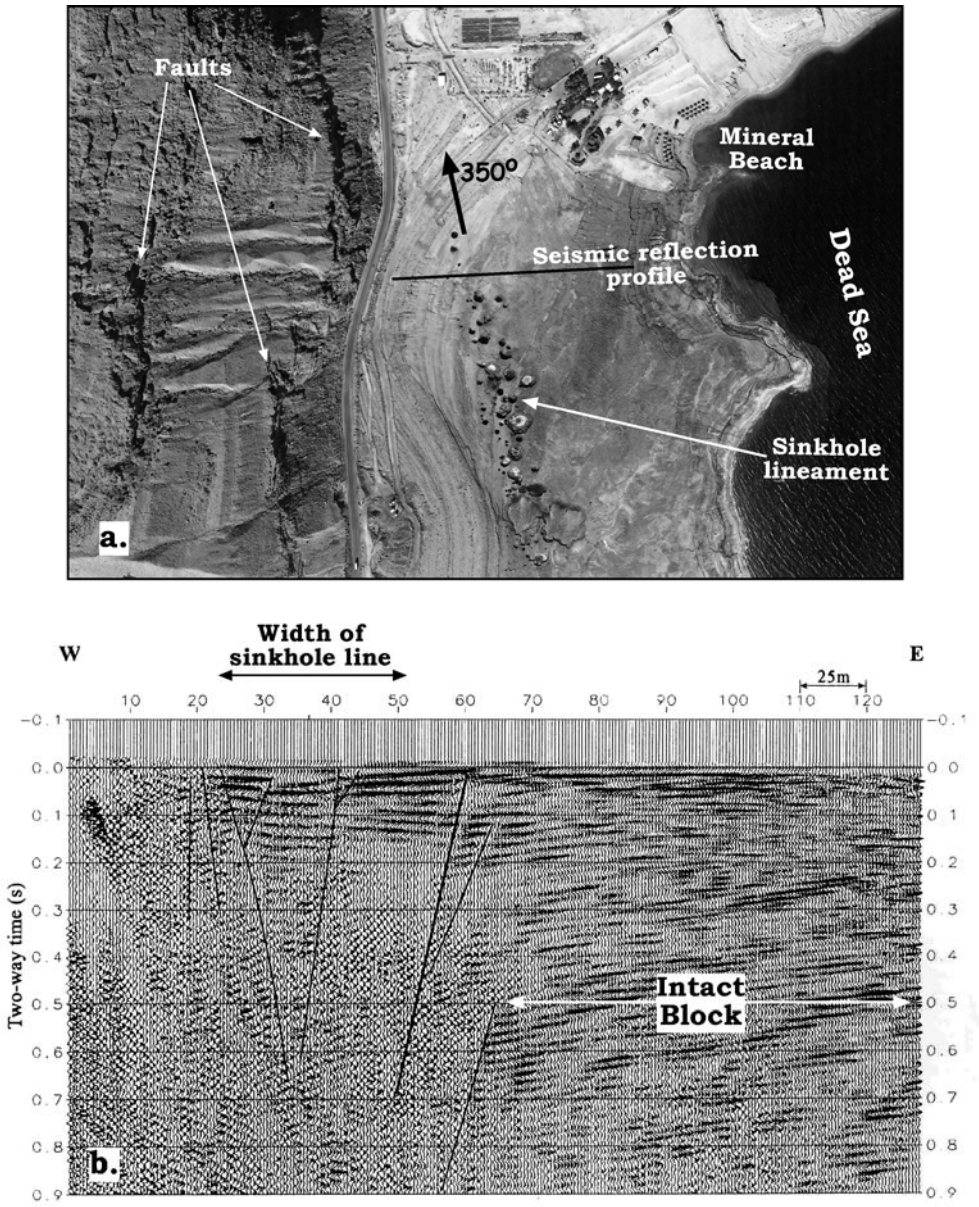

Figure 6: Sinkhole lineament and buried faults at the sinkhole site near Mineral beach (after Abelson et al., 2006). (a) A rectified air photograph from 2001 showing one of the sinkhole sites – Shalem site (Fig. 1 for location). The sinkholes are aligned sub-parallel to the local rift-margin faults. (b) Seismic reflection profile across the sinkhole line (profile location is marked in (a)) showing prominent discontinuities beneath the sinkhole lineament interpreted as faults, and intact structure of reflectors away from the sinkhole lineament.

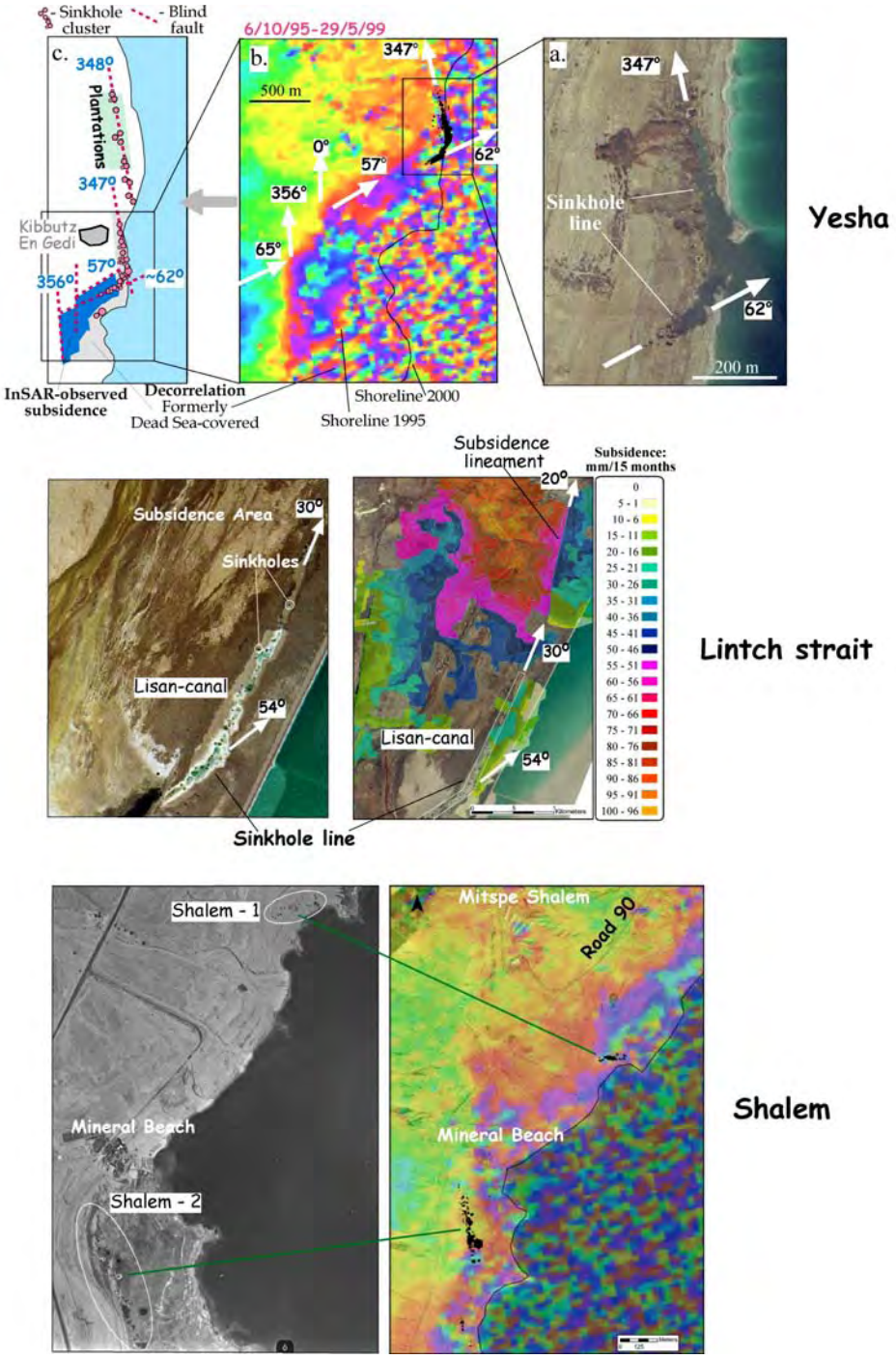

Figure 7: The buried tectonic fabric as revealed by sinkhole lines and InSAR-detected gradual subsidence in three various sinkhole sites (after Yechieli et al., 2004). *Upper panel*: (a) A rectified aerial photo showing a sinkhole site with two main linear segments. (b) A rectified interferogram displaying a subsiding area with straight boundaries suspected to be faults. The color fringe pattern in the interferogram reflects ground subsidence, where one fringe cycle represents ~31 mm of vertical displacement [*Baer et al.*, 2002]. (c) A schematic sketch showing our interpretation of the concealed tectonic fabric as inferred by the sinkhole lines and InSAR. Note that the straight borders of the subsidence area are sub-parallel to the sinkhole lines, and the N62°E striking sinkhole line is at the continuation of the step-shaped border of the subsiding area. This geometry is observed in all pairs of interferograms of this area (see Fig. 6 of *Baer et al.* [2002]). *Middle panel*: A sharp lineament partitions two areas of different subsidence rate calculated from the InSAR (right). This lineament is at the continuation and the same orientation of a 2 km long sinkhole-lineament. Both lineaments are probably surface expression of hidden faults. *Lower panel*: Parallelism between two sinkhole lineaments near Mineral beach and linear boundaries of a subsiding area.

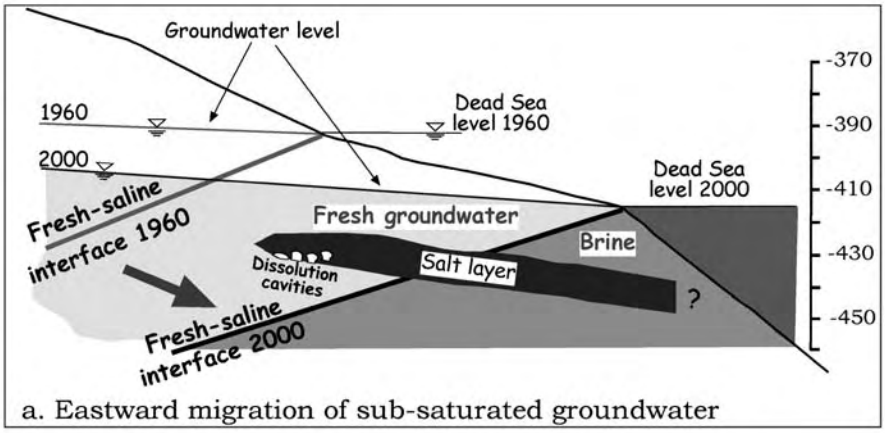

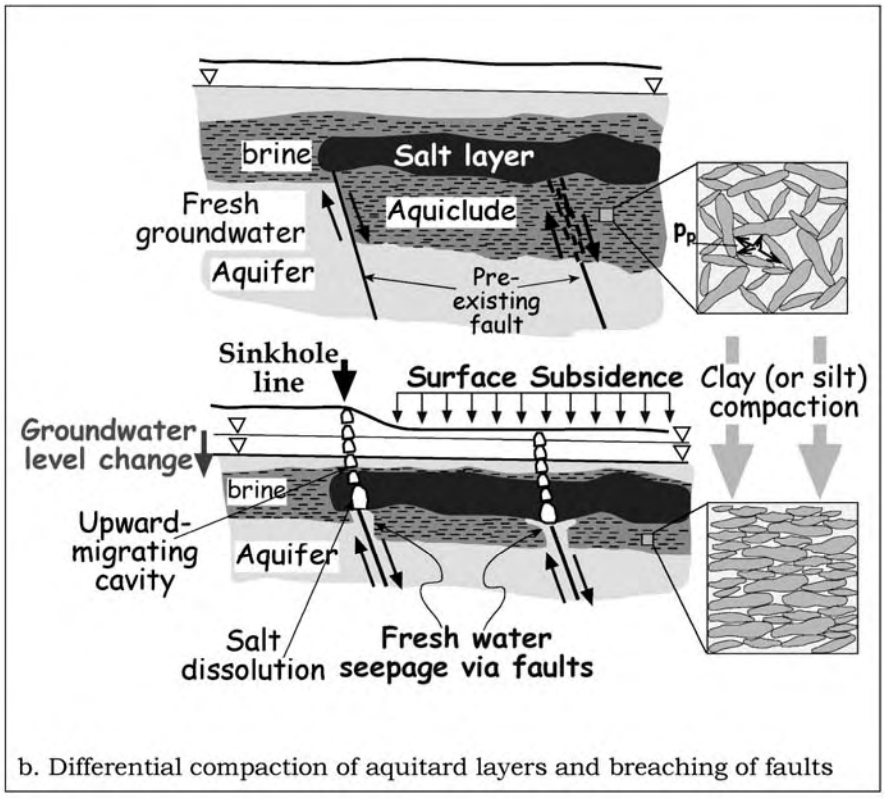

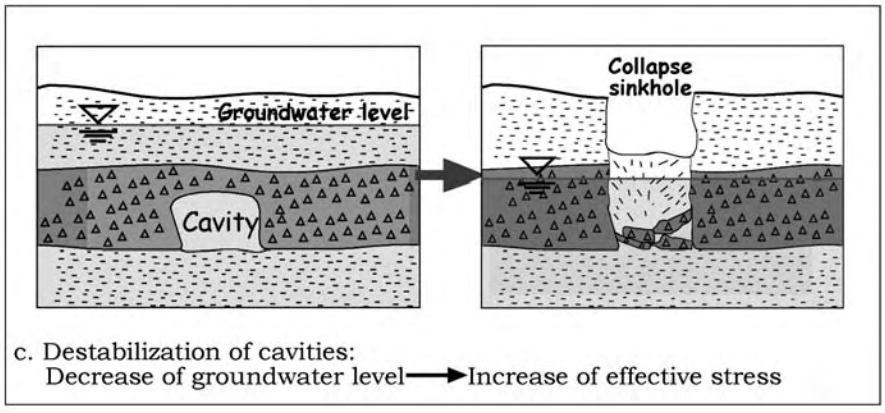

Figure 8: The triple effect of the decline of the Dead Sea level (After Abelson et al., 2006). Effects (a) and (b) cause cavity formation, while (c) is a catalyst for cavity collapse.

Figure 9: Two aerial photographs of the sinkhole sites near Mineral beach (Shalem-2) taken in January 2005 and December 2008. White arrow in both photos marks the northern tip of the sinkhole lineament in January 2005, and black arrow marks the northern tip in December 2008. The site growth was by development of sinkholes by lineament prolongation northward, and with some widening eastward. The sinkhole lineament lies above the western boundary of the salt layer (Fig. 4), where further salt dissolution forming more caverns causes the lineament widening eastward. Exposed fault escarpments are marked, and are oriented parallel to the sinkhole lineament (Fig. 6).

References

Abelson, M., Baer, G., Shtivelman, V., Wachs, D., Raz, E., Crouvi, O., Kurzon, I., and Yechieli, Y., 2003, Collapse-sinkholes and radar Interferometry reveal neotectonics concealed within the Dead Sea basin, *Geophysical Research Letters*, 30, v. 10, 1545, 52(1-4).

Abelson, M., Yechieli, Y., Crouvi, O., Baer, G., Wachs, D., Bein, A., and Shtivelman, V., 2006, Evolution of the Dead Sea sinkholes, in "New Frontiers in Dead Sea Paleoenvironmental Research", eds. Y. Enzel, A. Agnon, M. Stein, *Geological Society of America, Special Paper*, 401, 241-253.

Amelung, F., D.L. Galloway, J.W. Bell, H.A. Zebker, and R.J. Laczniak, 1999, Sensing the ups and downs of Las Vegas: InSAR reveals structural control of land subsidence and aquifer-system deformation, *Geology*, *27* (6), 483-486.

Baer, G., Schattner, U., Wachs, D., Sandwell, D., Wdowinski, S., and Frydman, S., 2002, The lowest place on Earth is subsiding - An InSAR (interferometric synthetic aperture radar) perspective, *Geological Society of America Bulletin*, 114 (1), 12-23.

Hall, J., (1994) Digital shaded map of Israel, Israel Geological Survey.

Galloway, D.L., K.W. Hudnut, S.E. Ingebritsen, S.P. Phillips, G. Peltzer, F. Rogez, and P.A. Rosen, 1998, Detection of aquifer system compaction and land subsidence using interferometric synthetic aperture radar, Antelope Valley, Mojave Desert, California, *Water Resour. Res.*, *34*, 2573-2586.

Sagy, A., Reches, Z., Agnon, A., 2003. Hierarchic three-dimensional structure and slip partitioning in the western Dead Sea pull-apart. Tectonics. V. 22 1004, doi:10.1029/2001TC001323

Shalev, E., Lyakhovsky, V., and Yechieli, Y., 2006, Salt Dissolution and Sinkhole Formation along the Dead Sea Shore, *J. Geophys. Res.*, 111, doi: 10.1029/2005JB004038.

Terzaghi, K., 1925. Principle of soil mechanics, V - Settlement and consolidation of clay, *Engineering News-Record*, *95*, 874-878.

Yechieli, Y., Abelson, M., Bein, A., Stivelman, V., Crouvi, O., Wachs, D., Baer, G., Kalvo, R. and Lyakhovsky, V., 2004. Formation of sinkholes along the shore of the Dead Sea – summary of finding from the second stage of research: Geological Survey Report GSI/41/2004 (in Hebrew), 34 p.

Yechieli, Y., Abelson, M., Bein, A., Crouvi, O., Shtivelman, V., 2006, Sinkhole "swarms" along the Dead Sea coast: Reflection of disturbance of lake and adjacent groundwater systems, *Geological Society of America Bulletin*, v. 118, 1075-1087.

Ze'elim Gully - a high –resolution lacustrine paleoseismic record of the late Holocene Dead Sea basin

Elisa Kagan[1],[2*] Revital Bookman[3*] Moti Stein[2*] Amotz Agnon[1]

1 Institute of Earth Sciences, The Hebrew University of Jerusalem
2 Geological Survey of Israel
3 Charney School of Marine Sciences, University of Haifa

elisa.kagan@mail.huji.ac.il

*Field guide

Introduction

During the last decades the Dead Sea has retreated from around 400 to around 430 m below MSL (BSL). The dramatic (mainly man–made) retreat has lead to the formation of new erosional gullies within the shore terraces, where the lacustrine sections of late Holocene Dead Sea are exposed, interfingered with fluvial and shoreline deposits. The sediments, composing the top of the Ze'elim Formation, contain deformed sequences (breccias and liquefied sands) that are interpreted as seismites. The seismites can be dated by radiocarbon to produce a chronology of seismic events in the region. This record is compared and combined with the historical record of earthquakes in the region, producing a high resolution paleoseismic record of the late Holocene time, which is used to constrain temporal and spatial occurrence patterns of earthquakes in the region. In this field trip we will see the deformation within the lacustrine sediments, present their dating, and discuss historical correlation. The landscape in this arid environment is responding rapidly to the developing base level and stations 2-5 described below represent a highly ephemeral setting.

Station 1 – Ze'elim Plain

We will stand on the margins of the Ze'elim Wadi fan-delta on sediments that emerged since the 1960s. This location was underwater for long periods of time during the Holocene, recording the lake's paleolimnological history. Ongoing erosion processes exposed the lacustrine sections that are currently more than 10 m thick and cover more than the past 5000 years (fig. 1).

The benefits of this location include relatively high sedimentation rates and abundant organic debris present in the sediments; both of which are favorable for high-resolution chronological and paleoseismological studies.

Station 2 – Gully B, southern wall

The gully wall (gully B, (Ken-Tor et al., 2001) is composed of fine grained to pebble units that indicate variations in the Dead Sea level in the past. Towards the east the facies become finer, representing a deeper off-shore depositional environment.

Deformation in a sandy unit indicates liquefaction during an earthquake event (fig. 2). Remains of the original bedding are visible. The deformation thins out to the west and eventually disappears. A thin undeformed layer separates two seismic events. In places the older event is "masked" by the younger one. This phenomenon points to the incompleteness of the record. Detection resolution for consecutive events is given by Tres=Hb/Rs, where Tres is the temporal resolution of individual earthquakes, Hb is the thickness of the breccia formed by the younger earthquake, and Rs is the rate of sedimentation (Agnon et al., 2006).

Organic debris deposited within the sediments before deformation were used for radiocarbon dating. Transport time of fine debris as small branches, stalks, and seeds into the lake with the seasonal flash floods is conceivably short; hence they can be used to date the seismic event. Most of the correlated historical earthquakes fall well within the 1σ error envelope of the seismite radiocarbon age (Ken-Tor et al., 2001; Agnon et al., 2006).

Station 3 – Gully B, northern wall

The uppermost section includes the youngest reported earthquakes in the region. The two seismites recognized in the exposure are separated by a few centimeters of lacustrine aragonite sediments that are correlated with the Dead Sea high stand of the late 19th century (when the lake rose to 392 m BSL). Radiocarbon dating, stratigraphic considerations, and historical documentation lead to the conclusion that these seismites record the 1834 and 1927 earthquakes.
Historical evidence for damage indicates the 1834 event epicenter was probably south of the Dead Sea. Alternatively, the M7.0 1837 earthquake from the Roum Fault in southern Lebanon (Ambraseys, 1997; Nemer and Meghraoui, 2006) could have re-disturbed the sediments. The M6.2 1927 earthquake was the first large seismic event to be recorded instrumentally. Its epicenter was re-located at the northern basin of the lake (Avni et al., 2002).

Station 4 - Gully A, Southern wall

Two nearby outcrop sections (western: ZA-1, Ken-Tor et al, 2001a and eastern: ZA-2, (Kagan et al., 2006) were described and 14C dated (34 radiocarbon ages) allowing the compilation of a relatively highly detailed paleoseismic record that was correlated to historical earthquakes. The sediments were deposited mostly in the lacustrine environment with occasional shore deposits (sandy units, aragonite crusts, and shore ridges) indicating lake level drops. The seismites here are mostly brecciated lacustrine laminae (fig. 3). The western section includes several depositional hiatuses. Missing earthquakes according to the historical record are correlated to the time intervals of these hiatuses. Indeed, where the lacustrine record is more complete, e.g. in the Ein Gedi, Ein Feshkha, and the recently studied east Ze'elim section, most of the historical records are well correlated with the seismites (Migowski et al., 2004; Neumann et al., 2007; Kagan et al., in preparation)
The more eastern section was dated by radiocarbon ages of organic debris by accelerator mass spectrometry (AMS) (Neumann et al., 2007). Modeling was carried out by Bayesian statistical methods using the OxCal-04 program (Bronk-Ramsey, 2008) for a depositional model (Kagan et al., in preparation). Six radiocarbon ages (no outliers) are available from ~1000 BC to 1500 AD (fig. 4).

Ten seismite ages were interpolated from the model based on their depths. Historical earthquakes were assigned to each of the seismites and fit within their 1σ age range.

Station 5 – Near the widening of Gully B, southern wall

Here we documented the famous 31 BC earthquake described in the Jewish wars of Flavius. The seismite comprises brecciated clayey detrital laminae, where 20 meters to the west it undergoes a facies change and is visible as liquefied sand. This earthquake was documented by other paleoseismic studies elsewhere along the DST (Reches and Hoexter, 1981; Migowski et al., 2004).

References

Agnon, A., Migowski, C., and Marco, S., 2006, Intraclast breccia layers in laminated sequences: recorders of paleo-earthquakes, in Enzel, Y., Agnon, A., and Stein, M., eds., New Frontiers in Dead Sea Paleoenvironmental Research, Geological Society of America Special Paper 401, p. 195-214.

Ambraseys, N.N., 1997, The earthquake of 1 January 1837 in Southern Lebanon and Northern Israel: Annali di Geofisica, v. XL, p. 923-935.

Avni, R., Bowman, D., Shapira, A., and Nur, A., 2002, Erroneous interpretation of historical documents related to the epicenter of the 1927 Jericho earthquake in the Holy Land: Journal of Seismology, v. 6, p. 469-476.

Bookman (Ken-Tor), R., Enzel, Y., Agnon, A., and Stein, M., 2004, Late Holocene lake levels of the Dead Sea: Geol Soc Am Bull, v. 116, p. 555-571.

Bronk-Ramsey, C., 2008, Deposition models for chronological records: Quaternary Science Reviews, v. 27, p. 42.

Kagan, E.J., Stein, M., Agnon, A., and Neumann, F., 2006, New observations from paleoseismic records across the Dead Sea and Jordan valley basins during the last 70,000 years, Geological Society of Israel annual meeting: Bet-Shean.

Ken-Tor, R., Stein, M., Enzel, Y., Agnon, A., Marco, S., and Negendank, J.F.W., 2001, Precision of calibrated radiocarbon ages of historic earthquakes in the Dead Sea Basin: Radiocarbon, v. 43, p. 1371-1382.

Migowski, C., Agnon, A., Bookman, R., Negendank, J.F.W., and Stein, M., 2004, Recurrence pattern of Holocene earthquakes along the Dead Sea transform revealed by varve-counting and radiocarbon dating of lacustrine sediments: Earth and Planetary Science Letters, v. 222, p. 301.

Nemer, T., and Meghraoui, M., 2006, Evidence of coseismic ruptures along the Roum fault (Lebanon): a possible source for the AD 1837 earthquake: Journal of Structural Geology, v. 28, p. 1483-1495.

Neumann, F.H., Kagan, E.J., Schwab, M.J., and Stein, M., 2007, Palynology, sedimentology and palaeoecology of the late Holocene Dead Sea: Quaternary Science Reviews, v. 26, p. 1476.

Reches, Z., and Hoexter, D.F., 1981, Holocene seismic and tectonic activity in the Dead Sea area: Tectonophysics, v. 80, p. 235.

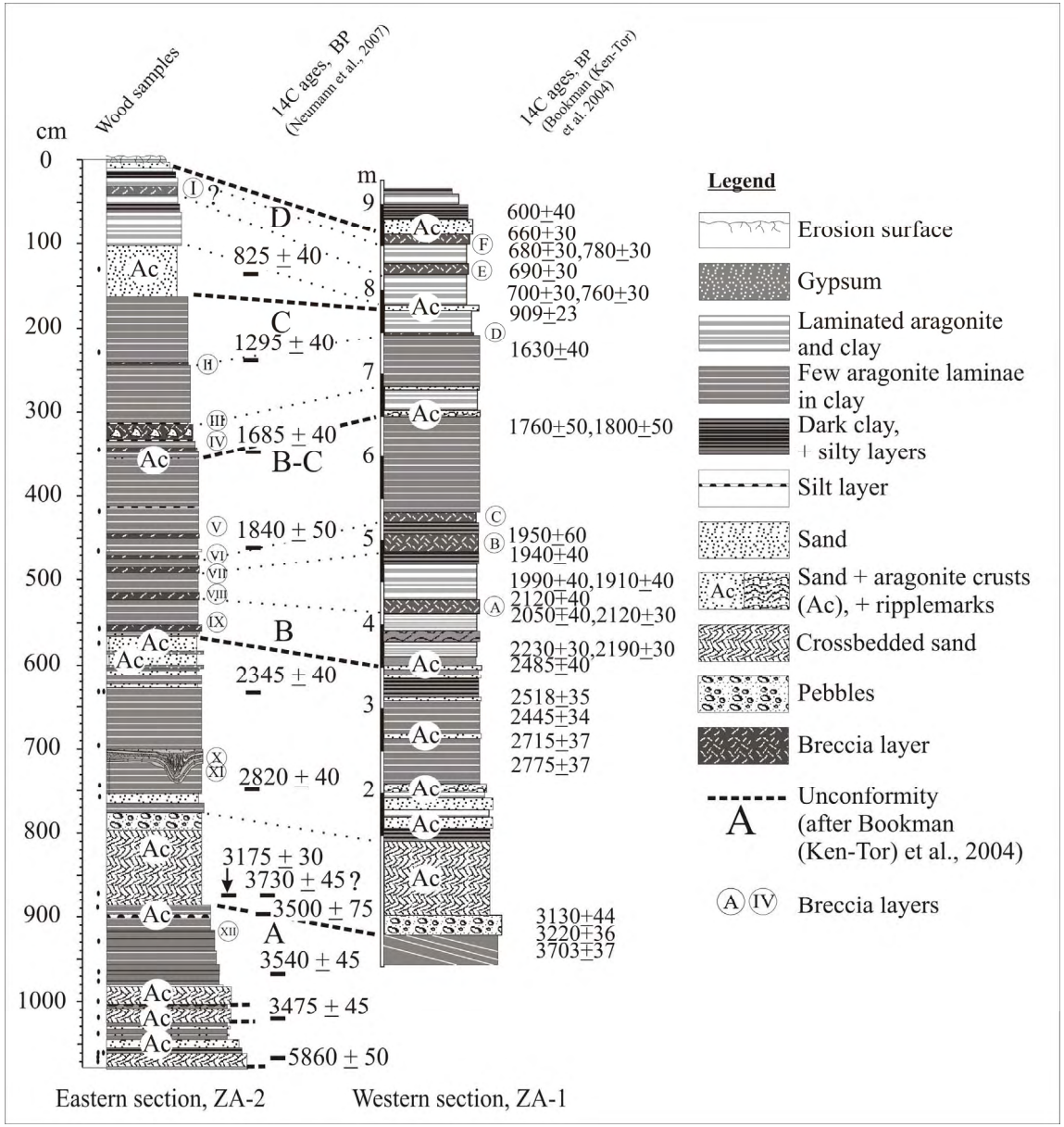

Figure 1: Eastern (left) and western (right) Ze'elim gully sections (diagram modified after Neumann et al., 2007). Radiocarbon ages (uncalibrated), seismites, and sedimentary unconformities are marked.

Figure 2: Photograph of liquefied sand from Ze'elim Gully B.

Figure 3: Photograph of intraclast brecciated layer, Ze'elim Gully A. Note dark grey matrix with broken fragments of aragonite laminae. Dated to the 31BC earthquake documented by Flavius.

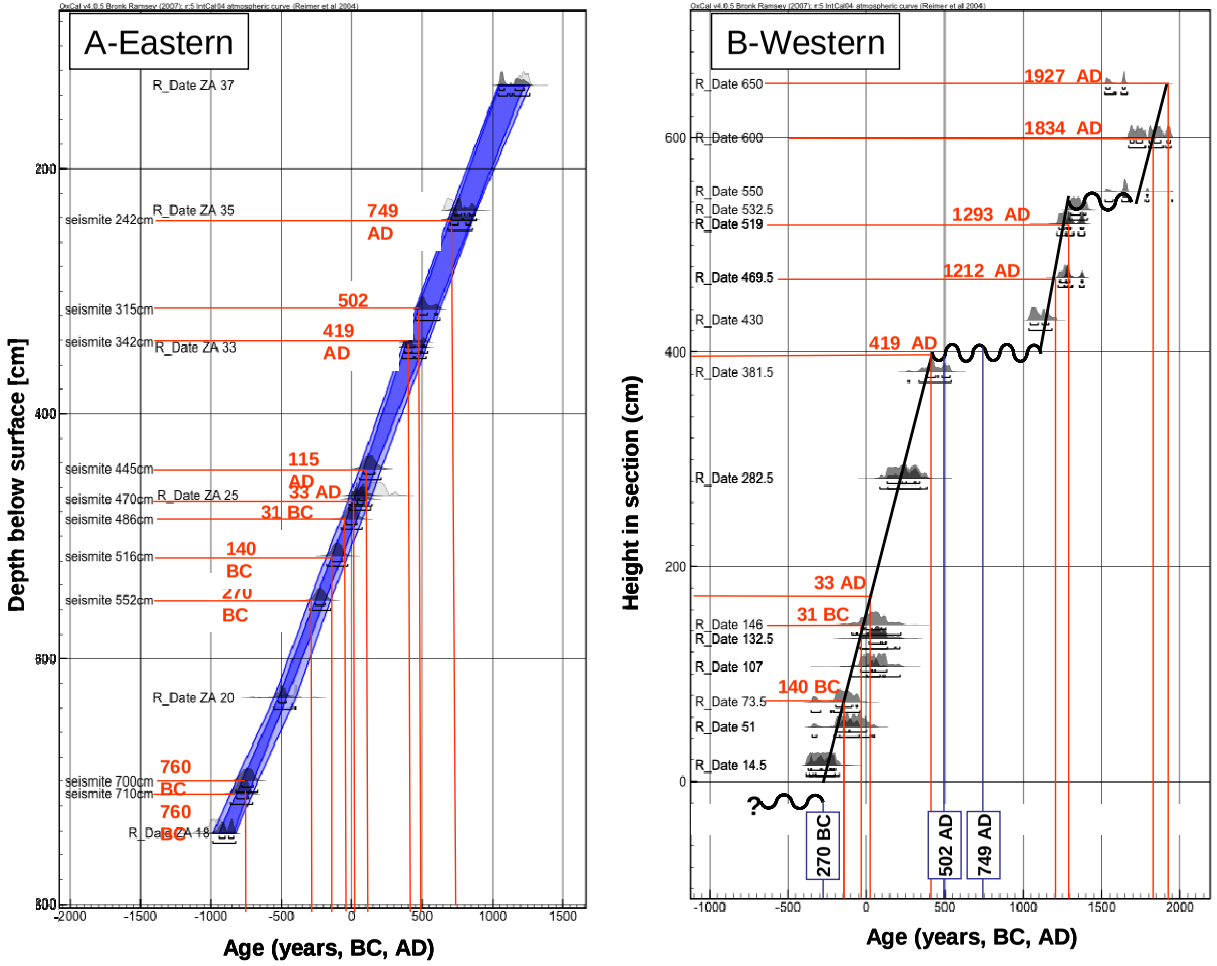

Figure 4: Age-depth models of Ze'elim sections. (a) ZA-2, eastern section, deposition model according to OxCal04 P_sequence. Outer (light blue) range gives 2s, inner (dark blue) range gives 1s model ages. Date histograms indicate calibrated and modeled ages of radiocarbon samples. Seismite histograms from marked depths (i.e. seismite 552cm) indicate model ages of seismites. (b) ZA-1, radiocarbon data and historical correlation, modified after Ken-Tor et al. (2001) and Agnon et al. (2006). Diagonal black lines define periods of deposition. Horizontal curvy lines define depositional hiatuses, which correlate to lake level drops. Blue lines and dates at X-axis are earthquakes which occurred during depositional hiatuses and are missing in the western record but appear in the eastern record.

High-resolution stratigraphy reveales repeated earthquake faulting in the Masada Fault Zone, Dead Sea Transform

Shmuel Marco[1]*, Amotz Agnon[2]

[1]Department of Geophysics and Planetary Sciences,Tel Aviv University, Israel

[2]Institute of Earth Sciences, The Hebrew University of Jerusalem

amotz@cc.huji.ac.il

*Field guide

A syndepositional fault zone east of Masada provides an example for fundamental characteristics of earthquakes, such as long term temporal clustering, repeated faulting on the same planes for a limited time of the order of a few thousands of years, and the formation of subaqueous breccia layers interpreted as seismites. The MFZ was studied in outcrops of Lake Lisan sediments, dated by the Uranium series to 70-15 ka (Schramm et al., 2000). Detailed columnar sections on both sides of well-exposed faults show that each individual fault exhibits a cluster, up to 4 kyr long, with 3-5 slip events on the same plane. Each slip event is associated with the formation of widespread layers exhibiting soft sediment deformation, which are interpreted to be seismite layers. The uppermost part of the Lisan section, about 5 m, is not faulted, hence the last cluster of slip events, ended about 25 kyrs ago. The clusters of activity of individual faults coalesce to form larger clusters. These are evident in the distribution of seismite layers throughout the entire Lisan section which shows earthquake clustering during periods of ~10 kyr. The clusters are separated by relatively quiescent periods of comparable duration (Agnon et al., 2006; Marco and Agnon, 2005; Marco et al., 1996).

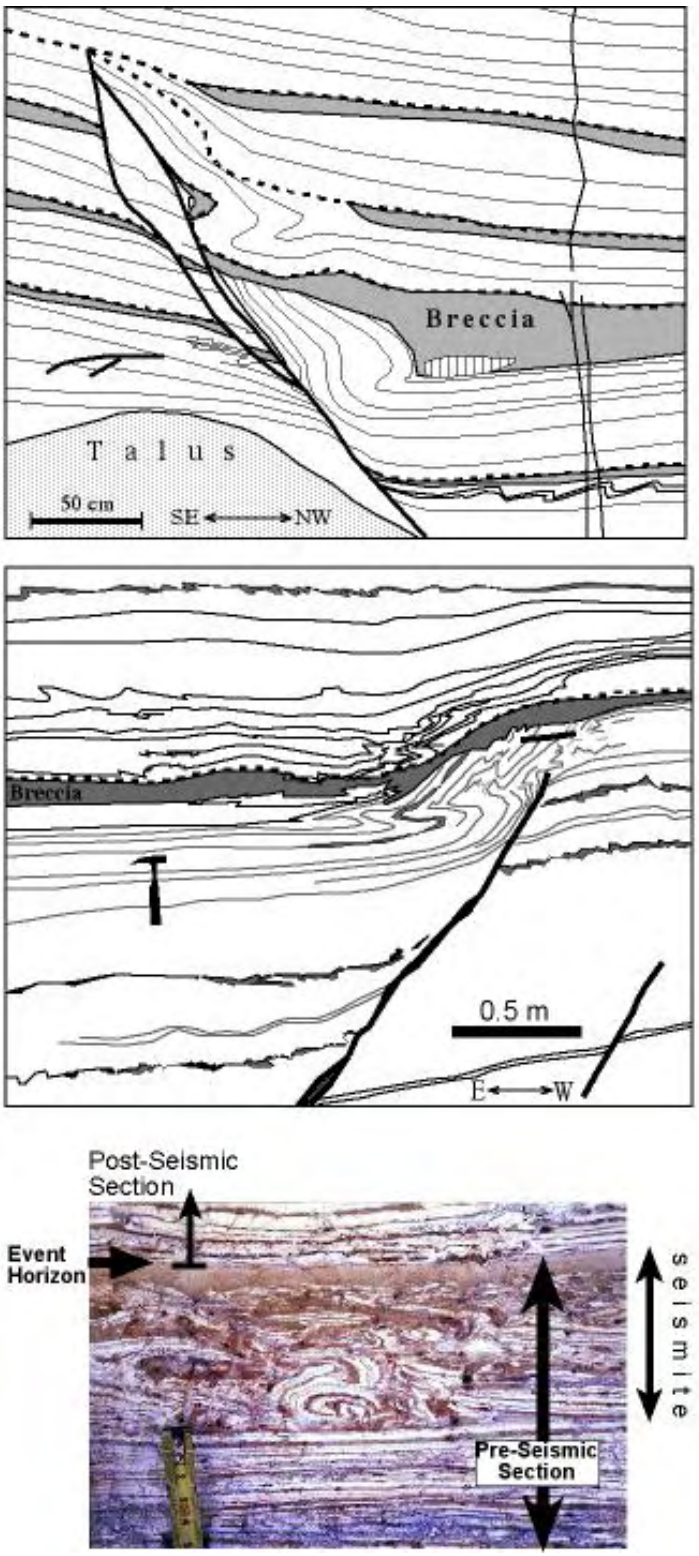

Figure 1: Typical syndepositional fault exposures. Top two: Line drawings are traced from photographs, emphasizing bedding, breccia layers (gray), and fault planes (solid lines). The association of faults and breccia layers indicates that the latter formed when slip occurred on the fault. Dashed thick lines are traces of the surfaces immediately after slip events, i.e., event horizons. One of the breccia layers in exposure 16 contains an embedded intraclast with vertical laminae. It probably fell from the adjacent fault scarp. Photograph at bottom shows a 7-cm-thick breccia layer exhibiting large fragments of former laminas at the

bottom and upward decrease of fragment size. The top of the breccia layer is made of pulverized laminae. We interpreted such layers as seismites, which have been formed by fluidization of upper part of the sediment at the bottom of the lake during strong earthquake shaking (Marco and Agnon, 1995).

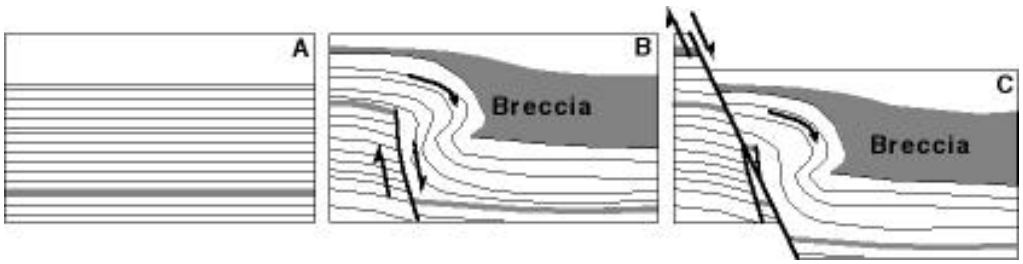

Figure 2: A model of subaqueous faulting that explains the observed faults. **A.** Horizontal laminated sediment at the bottom of the lake. **B.** Faulting forms a scarp (solid line) and the shaking triggers the formation of a breccia layer composed of a mixture of laminated fragments at the top of the sediment. The breccia layer is thicker in the hanging wall. Reclining folds in the hanging wall form coseismically when uppermost poorly consolidated layers slump down the fault scarp. **C.** A second slip event.

References

Agnon, A., Migowski, C., and Marco, S., 2006, Intraclast breccia layers in laminated sequences: recorders of paleo-earthquakes, *in* Enzel, Y., Agnon, A., and Stein, M., eds., New Frontiers in Dead Sea Paleoenvironmental Research, Geological Society of America Special Publication, p. 195-214.

Marco, S., and Agnon, A., 1995, Prehistoric earthquake deformations near Masada, Dead Sea graben: Geology, v. 23, p. 695-698.

Marco, S., and Agnon, A, 2005, High-resolution stratigraphy reveals repeated earthquake faulting in the Masada Fault Zone, Dead Sea Transform: Tectonophysics, v. 408, p. 101-112.

Marco, S., Stein, M., Agnon, A., and Ron, H., 1996, Long term earthquake clustering: a 50,000 year paleoseismic record in the Dead Sea Graben: J. Geophys. Res., v. 101, p. 6179-6192.

Schramm, A., Stein, M., and Goldstein, S.L., 2000, Calibration of the ^{14}C time scale to 50 kyr by ^{234}U-^{230}Th dating of sediments from Lake Lisan (the paleo-Dead Sea): Earth Planet. Sci. Lett., v. 175, p. 27-40.

Mor structure: example for Late Pleistocene north-south extension in the Dead Sea basin

Amir Sagy[1]*, Yuval Bartov[2]

[1]Geological Survey of Israel
[2] I.E.I Ltd.

asagy@gsi.gov.il

*Field guide

The Dead Sea basin

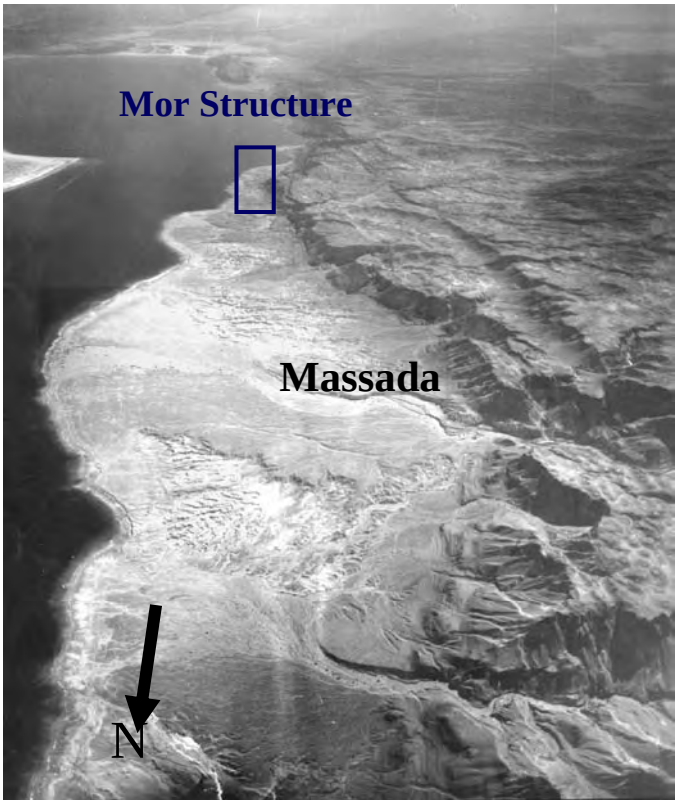

The Mor structure is a deformed zone located in the Dead Sea basin. Faults that are exposed in this location were active from Late Pleistocene times to the present. The structure includes E-W trending normal faults that are bounded and crossed by N-S trending faults. The well exposed fault system and the precise chronology of the regional Late Pleistocene deposits (Schramm, Stein & Goldstein, 2000; Bartov et al. 2002) have been used to calculate the amount, timing and rate of extension of the structure over the last 50 ka (Bartov & Sagy, 2004).

Mor structure: Stratigraphic section

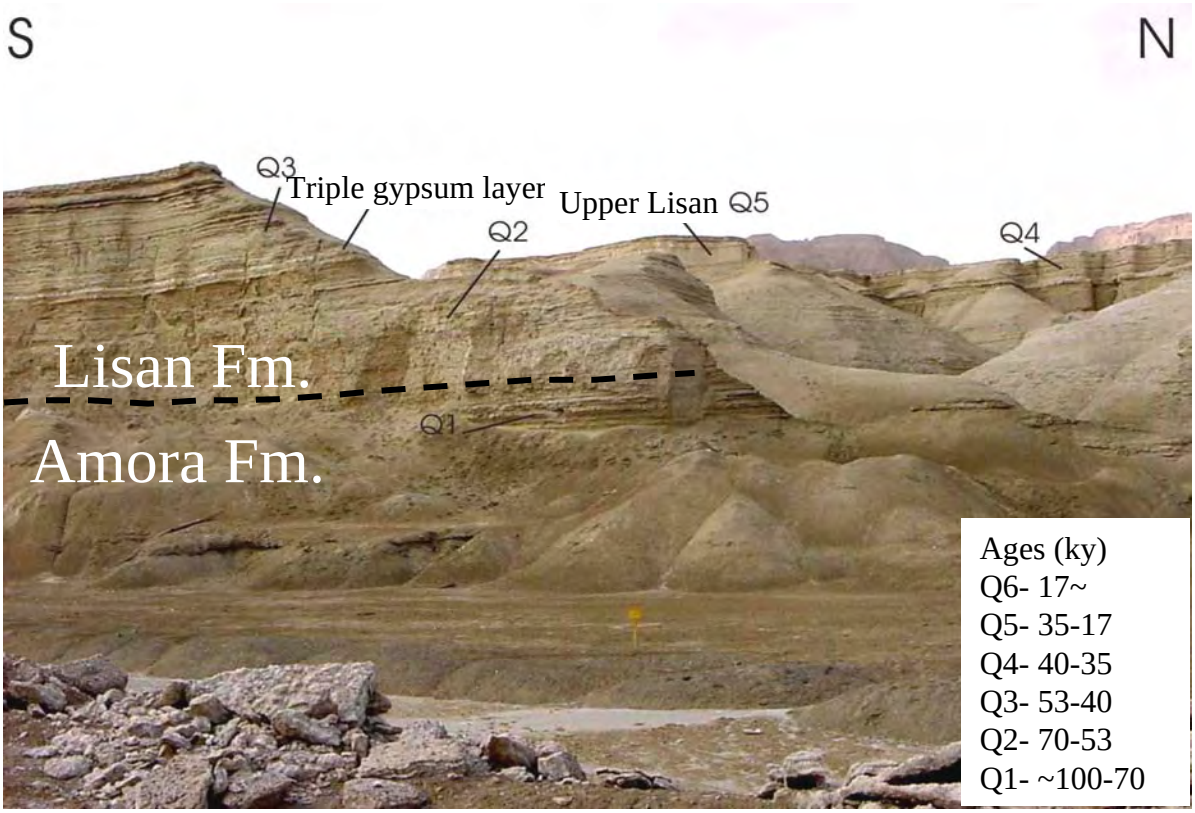

The Dead Sea Basin hosted a number of lacustrine water bodies since the Pliocene time (Stein, 2001). The exposed sedimentary sequences are mostly the remnants of Late Pleistocene to Holocene lakes (Amora, Lisan and Ze'elim), that are chronologically well constrained (Kaufman, Yechieli & Gardosh, 1992; Schramm, Stein & Goldstein, 2000; Waldman, 2002). The Mor structure is located at the distal part of the small Mor Valley fan delta. This geographic position produces a relatively continuous record of deposition interrupted by episodic low-lake levels that are expressed by distinct unconformities. The stratigraphic sequence consists of 37 m of laminated aragonite, silts and gypsum that interfinger with coarse clastic deposits transported from the western shores by streams. These deposits are of the Upper Amora (<120–70 ka) and Lisan formations (70–15 ka) and are partly covered by a thin transgressive Holocene unit (<6 ka). The local section is divided into six mapping units that are well correlated with high-resolution U–Th dated sections (Schramm, Stein & Goldstein, 2000; Bartov et al. 2002).

Mor Structure: Geological map

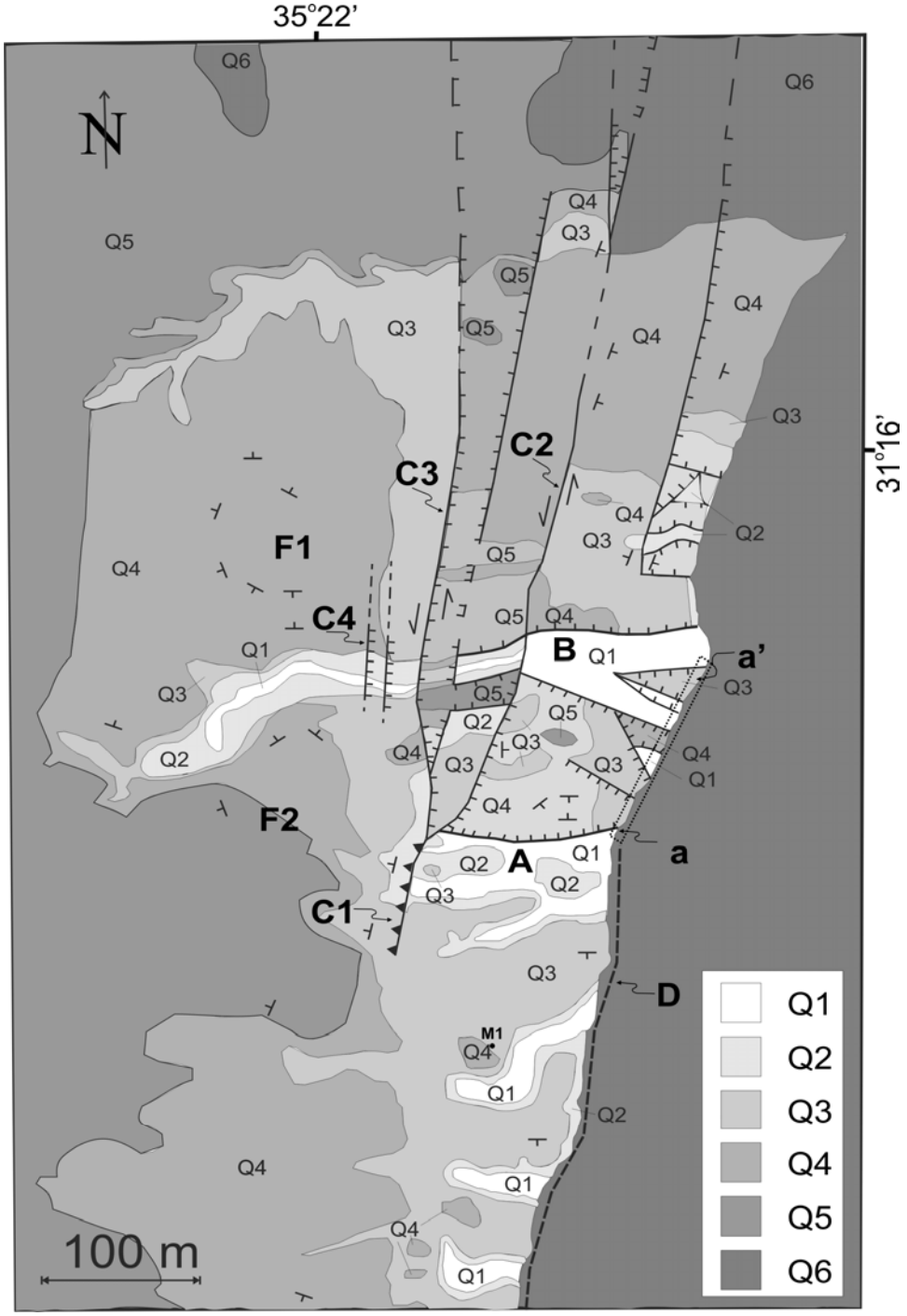

The Mor structure is bounded by N–S-trending faults, and cross-cut by low-angle, E–W-trending normal faults. The continuing deformation in this structure is evident by the observation of at least three deformation episodes between 50 ka and the present. The calculated extension is 3.5 mm/yr over the last 30 000 years.

Field observations: High and low angle normal faults

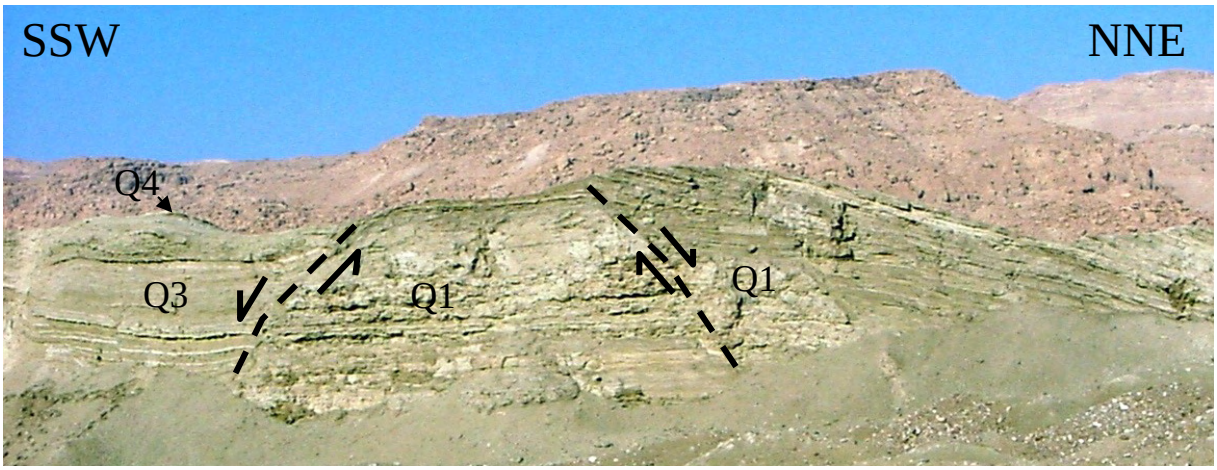

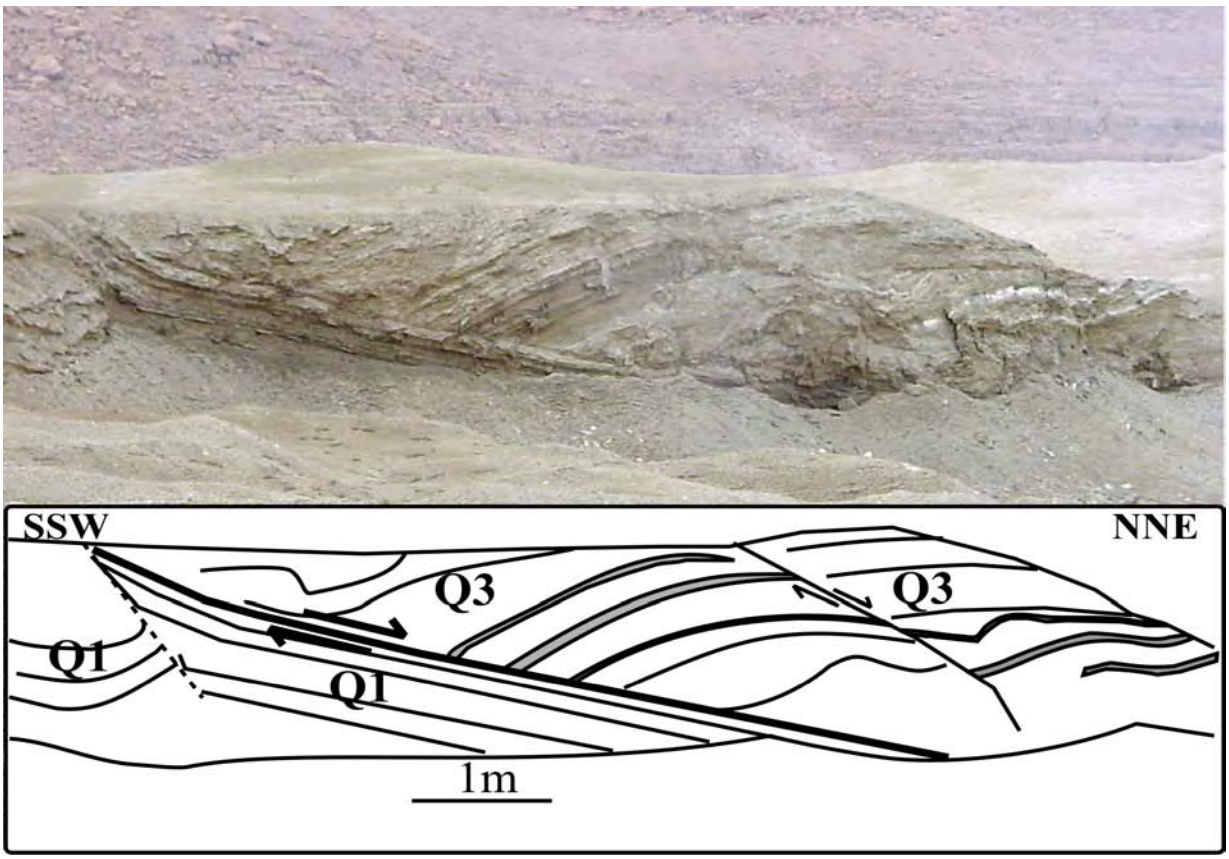

Faulting and ductile deformation on N-S trending faults

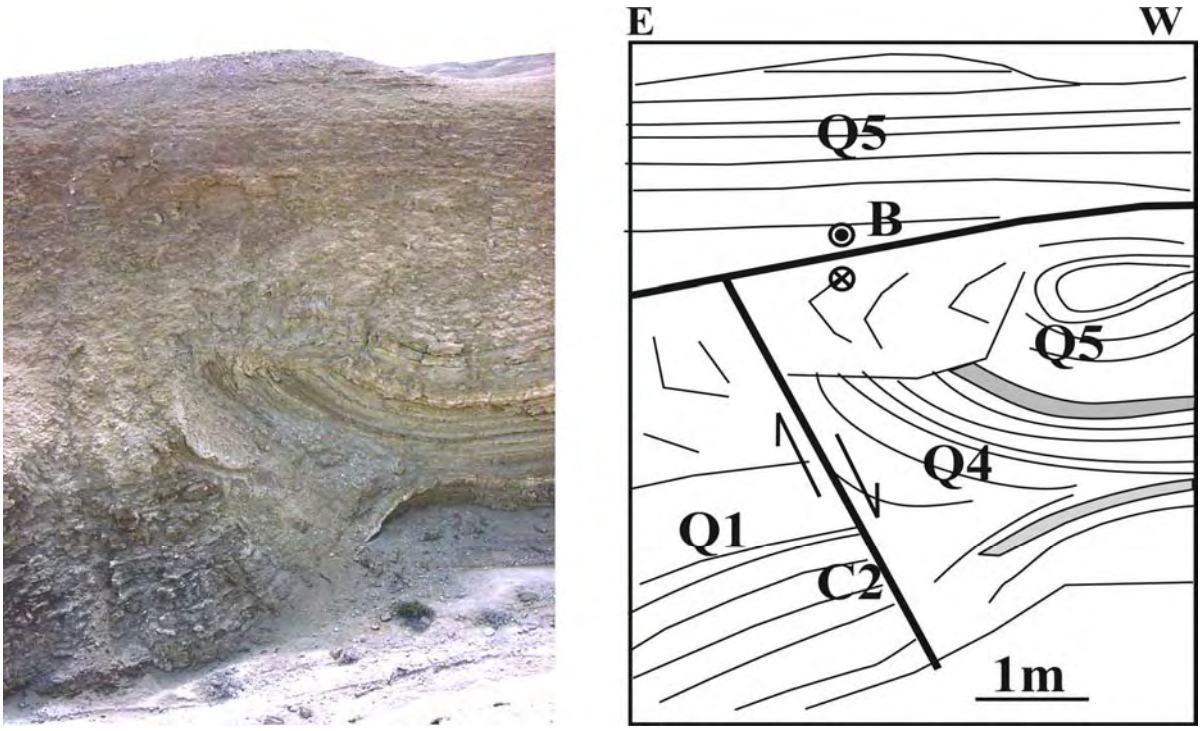

Elongated structural dome

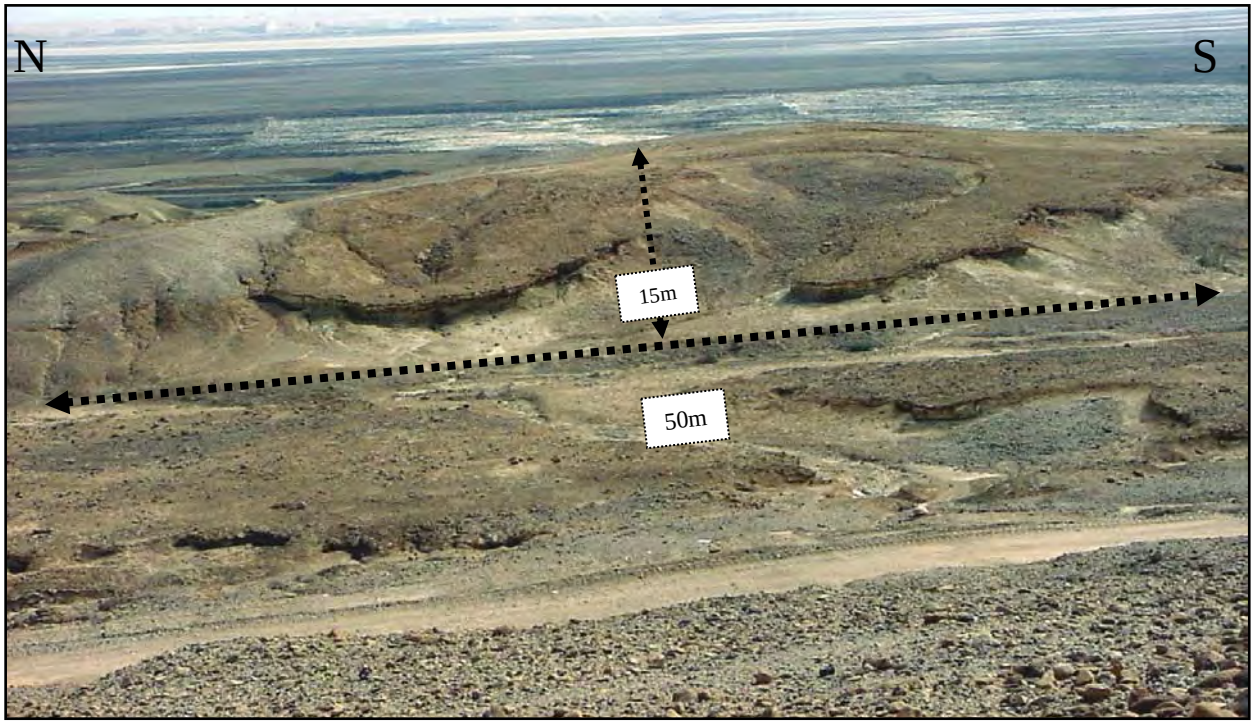

Mor structure: Interpretation

The N-S extension along the Mor structure is orthogonal to the dominant E–W extension within the western margins of the Dead Sea Basin (Sagy, Reches & Agnon, 2003), and thus it is best interpreted as associated with strike-slip motion along the N-S trending faults. Furthermore, a sinistral sense of motion along system C is indicated by: (1) a thick pebbly layer locally observed west of fault C in the dome's area is concealed at the southeastern part, and is exposed again some 70 m to the northeast of fault C; (2) the penecontemporaneous growth of the structural uplift west of the boundary longitudinal fault is consistent with observations in experiments of pull-apart development in ductile materials (Reches, 1988).

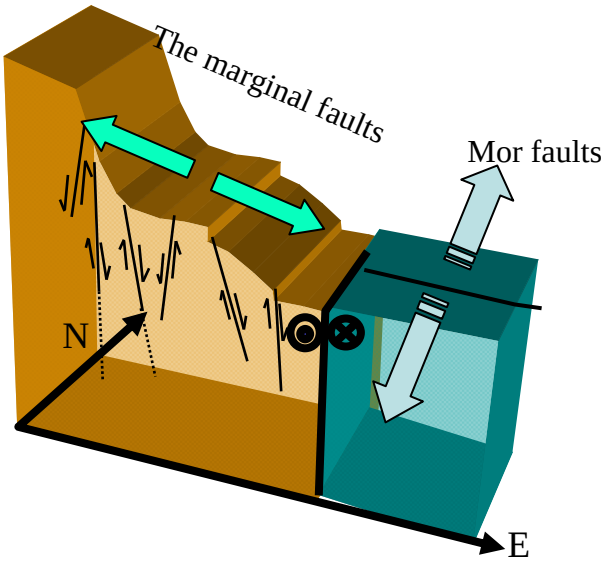

(3) recent seismic activity in the Dead Sea Basin indicates that four sinistral events occurred in the immediate proximity of the Mor structure over the past decade (Hofstetter et al., 2007).
The relationship between longitudinal faults and E–W normal faults suggests that the horizontal motion along the two stepped N–S strike slip faults is transferred from one to the other by the extension associated with the normal faults. Such relation lead us to interpret the structure as a small pull-apart in a strike slip system.

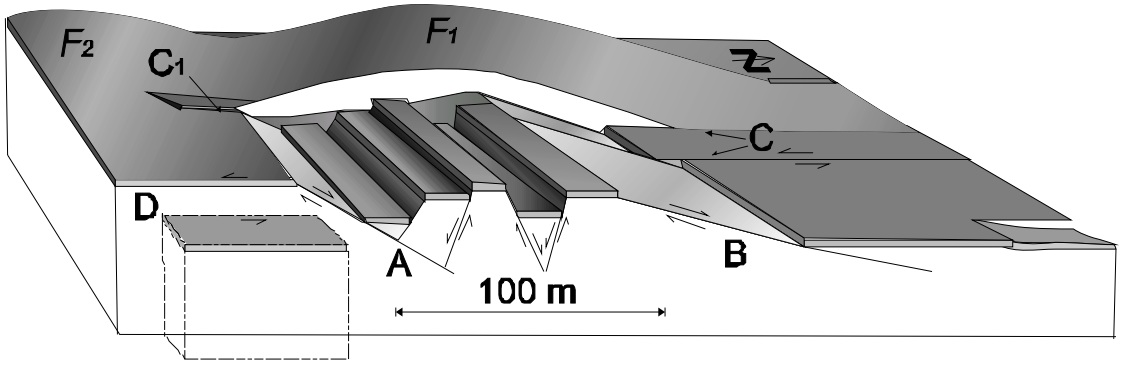

References

Bartov, Y., Stein, M., Enzel, Y., Agnon, A. & Reches, Z. 2002. Quaternary Research 57, 9–21.
Bartov, Y. & Sagy, A. 2004. Geological. Magazine. 141, 565–572.
Haase-Schramm, A., Goldstein, S. L. & Stein, M. 2004. Geochimica et Cosmochimica Acta 68, 985–1005.
Hofstetter R., Klinger Y., Abdel-qader A., Rivera L., & Dorbath L., 2007. Tectonophysics 429, 165-181.
Reches, Z. 1988. Tectonophysics 145, 141–56.
Sagy, A., Reches, Z. & Agnon, A. 2003. Tectonics 22.
Schramm, A., Stein, M. & Goldstein, S. L. 2000. Earth and Planetary Science Letters 175, 27–40.
Stein, M. 2001. Journal of Paleolimnology 26, 271–82.
Waldman, N. 2002. M.Sc. thesis, Hebrew Univ. Jerusalem,

Emplacement mechanism and fracture mechanics of clastic dikes

Tsafrir Levi[1]*, Ram Weinberger[1], Yehuda Eyal[2], Tahar Aïfa[3], Vladimir Lyakhovsky[1], Naomi Porat[1], Shmuel Marco[4], Eyal Heifetz[4]

1. Geological Survey of Israel
2. Department of Geological and Environmental Sciences, Ben Gurion University of the Negev
3. G´eosciences-Rennes, CNRS UMR6118, Universitee´ de Rennes l, Campus de Beaulieu, France
4. Department of Geophysics and Planetary Sciences, Tel Aviv University, Israel

tsafrir@gsi.gov.il

*Field guide

Clastic dikes are discordant, sub-vertical sheets of sediment within a host rock. While the common final geometry of these structures is everywhere similar and well defined, their mode of formation is ambiguous. This ambiguity arises because the sediment comprising the dikes may accumulate either 'passively' (depositional dikes) by deposition of clastic materials into preexisting fissures or 'dynamically' (injection dikes) by fracturing the country rocks and injection of clastic materials during overpressure buildup. Many studies of clastic dikes deal with the possible source rocks of the dike fill, but usually their determinations are either tentative or unequivocal. Only a few studies deal with the emplacement mechanism of the clastic dikes, but commonly without integrating the issues of fracturing with flow mechanics of clastic material and direction of flow.

To complete the paleoseismic record, all structures in seismically active zones that were induced by relative strong earthquakes should be identified. Of these structures injection dikes are probably the most impressive liquefaction-fluidization features that occur during relative large earthquakes (M>6.5). Hence, understanding the processes involved in dynamic clastic dike emplacement is of interest beyond the context of clastic transport. The present study focuses on the mechanisms of clastic-dike formation within the seismically active Dead Sea Fault (DSF) zone. The study area is located within the Ami'az Plain and Nahal Perazim area where hundreds of dikes cross-cut the late Pleistocene lake sediments of the Lisan Formation.

To understand the processes of clastic dike emplacement mainly two aspects were studied in the frame of the present work: (1) the transportation mechanism of the clastic material comprising the dikes; and (2) the fracture mechanics of the evolving dikes that enabled the injection of the clastic material into the host rock. In this study, independent techniques were used to differentiate between depositional dikes and injection dikes. One technique is based on Anisotropy of Magnetic Susceptibility (AMS) of the dike's fill. The AMS was applied here to detect the origin and shed light on the transportation of the clastic infill. The second technique used here was the Optically Stimulated Luminescence (OSL) dating method to distinguish between the depositional dikes and the injection dikes and to suggest reasonable interval ages for

the clastic dikes' emplacement. The third technique applied the Elastic Crack Theory (ECT) and the channel flow theory to the clastic dikes to understand the fracturing and the dynamics that took place during the dike emplacement. The fourth issue, though not one of the main issues of this study, is to understand the fracture mechanism of the clastic dikes by using the relations between the fracture apertures and the fracture heights (*A-H*) in 3-D and the sizes of the Elongated Tip Zone (ETZ) and comparing them with the Linear Elastic Fracture Mechanics (LEFM) theory (and other fracture mechanic theories).

In the present study the anisotropy of magnetic susceptibility (AMS) of clastic dikes of known origin was analyzed and the characteristic AMS signatures of depositional or injection filling was defined. The passively filled dikes, comprising brownish silt that resembles the local surface sediments, are characterized by an oblate AMS ellipsoid and vertical minimum susceptibility axis V_3. The dikes comprising green clayey sediment, which is connected to a mineralogically identical detrital layer in the Lisan Formation, are characterized by a triaxial AMS ellipsoid, well-grouped sub-horizontal and parallel to the dike walls' maximum susceptibility axis V_1, and sub-vertical intermediate susceptibility axis V_2. Field evidence and AMS analysis indicate that these dikes were emplaced by injection probably due to seismically triggered fluidization-liquefaction.

Detailed analyses of the magnetic fabric indicate that the clastic dikes formed by simultaneous fracture propagation and injection of clastic material into the fractures as a result of high pressure buildup in the source layer. The AMS results supported by field evidence indicate that the injection of clay-rich sediment is characterized by: (1) Vertical flow characterized by subvertical V2 axes, indicating the flow directions during fast flow, and subhorizontal V1 and V3 axes. and (2) Subvertical V3 axes characterizing horizontal slow flow, and subhorizontal V1 and V2 axes. A streaked AMS pattern mainly comprised of V2 and V3 axes represents a turbulent flow that generated local eddies during the clastic material transport. The AMS parameters along the dikes and possible grain imbrications along the dike walls support preferred orientation of grains under high strain rates. This novel application of the AMS provides a petrofabric tool for distinguishing passively filled dikes from injection dikes and identifying the latter as seismites.

The quartz single aliquot OSL ages of both depositional and injection dikes are between 15 and 7 ka, younger than the Lisan host rock. The highly scattered distribution of single grain ages of depositional dikes suggests several episodes of infill. The latest Pleistocene to Holocene single grain ages of the injection dikes results from the resetting of OSL signals because they do not contain recently bleached grains that infiltrated from above. The resetting occurred at the time of fluidization–liquefaction and buildup of fluid pressure within the injection dikes. If this resetting mechanism has a physical basis, then OSL dating is an important tool for constraining the ages of earthquake-induced injection dikes.

Two analytic models were examined based on field observations and experimental viscosity tests: (A) a channel flow for upward injection of a clay–water mixture; and (B) a profile of fracture dilation based on the elastic theory analysis. These two models predict that high

pressures, between 1-10 MPa, were generated in the dikes and source layer during the last stage of the injection process. The model of channel flow predicts that the injection velocity can reach tens of meters per second, and the emplacement time of the clastic dikes is on the order of a few seconds. The emplacement of the shallow clastic dikes in the Dead Sea basin could not have been driven by buoyancy. It is suggested that the high pressure values may result from the seismic waves which passed through the solid medium. The predicted high pressure values indicate that the clastic dikes were emplaced very close to an active segment of the Dead Sea Fault. The high pressures that lead to the injection process could also have caused the resetting of OSL ages as suggested above.

The present study suggests, based on field measurements and analysis of fracture geometry, that the small-scale fractures (clastic dikes) (height<1m), extensively developed in the upper Lisan Formation, belong to the last stage of the dynamic fracturing process. It is suggested that these fractures developed under deceleration conditions and have propagated at a post dynamic fracturing stage. Plotting the apertures and the fracture heights (*A-H*), measured in 3-D from different outcrops strongly indicate power-law relations. The present study shows that these power-law relations form only because fractures whose heights are less than 0.1m indicated a non constant aspect ratio (*A/H*). Because in these fractures the *A/H* is not constant, the LEFM theory in such fracture sizes can no longer hold and other fracture mechanic theories such as Elastic Plastic Fracture Mechanics (EPFM) should be used. The relative increase of the ETZ height may bring to increasing the resistance to fracturing. Since at this stage the ETZ height is relatively long, the stress intensity is estimated under an Elastic Plastic condition (Anderson, 1995). This condition lowers the stress intensity magnitudes and consequently the velocity is lowered as well. Based on the above, it is suggested that the formation of the ETZs may also play an important role in dynamic fracturing during the deceleration process; this must be further verified in the future.

References

Levi, T., Weinberger, R., Aïfa, T., Eyal, Y. & Marco, S., 2006a. Earthquake-induced clastic dikes detected by anisotropy of magnetic susceptibility: *Geology*, **34**, 69-72, doi: 10.1130/G-22001.1

Levi, T., Weinberger, R., Aïfa, T., Eyal, Y. & Marco, S., 2006b. Injection mechanism of clay-rich sediments into dikes during earthquakes. *Geochem. Geophys. Geosyst.*, **7**(2) 1–20, Q12009, doi:10.1029/2006GC001410.

Levi, T., Weinberger, R., Eyal, Y., Lyakhovsky, V., Heifetz, E &., 2008. Velocities and driving pressures of clay-rich sediments injected into clastic dykes during earthquakes: *Geophys. J. Int.*, 1-13, 10.1111/j.1365-246X.2008.03929.x.

Porat, N., Levi, T. & Weinberger, R., 2007. Possible resetting of quartz OSL signals during earthquakes—Evidence from late Pleistocene injection dikes, Dead Sea basin, Israel. *Quatern. Geochron.*, **2**, 272-277.

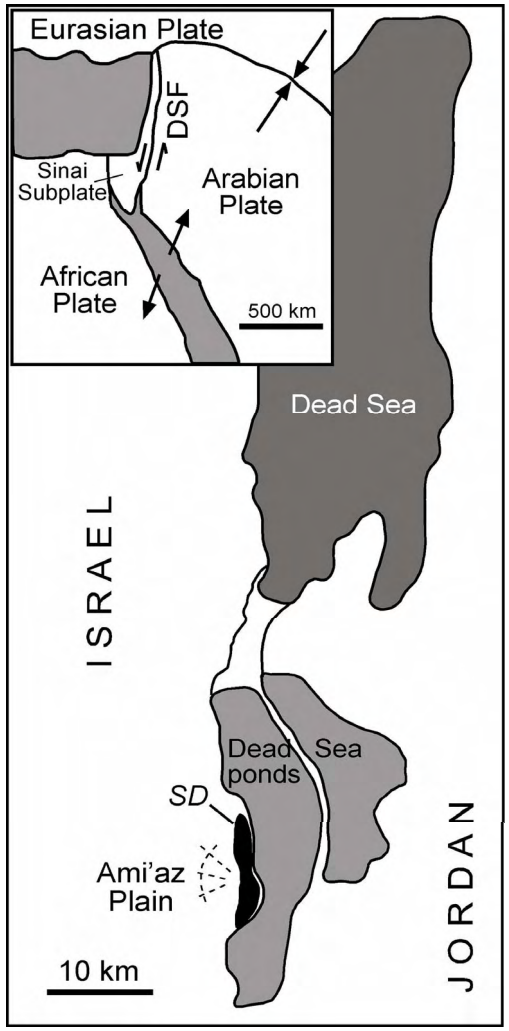

Figure 1: Location maps of the study area. The regional setting of the Dead Sea Fault (inset) and the Ami'az Plain with the clastic dikes marked schematically by dashed lines. DSF, Dead Sea Fault; SD, Sedom Diapir. The rocks exposed in the Ami'az Plain belong to the late Pleistocene Lisan Formation, which consists mostly of lacustrine laminae of aragonite and fine detritus, dated between ca. 70 and 14 ka (Haase-Schramm et al., 2004, and references therein). About 250 clastic dikes were mapped in the Ami'az Plain by means of aerial (after Levi et al., 2006a).
photographs and field surveys (Marco et al, 2002, Levi et al, 2006a).

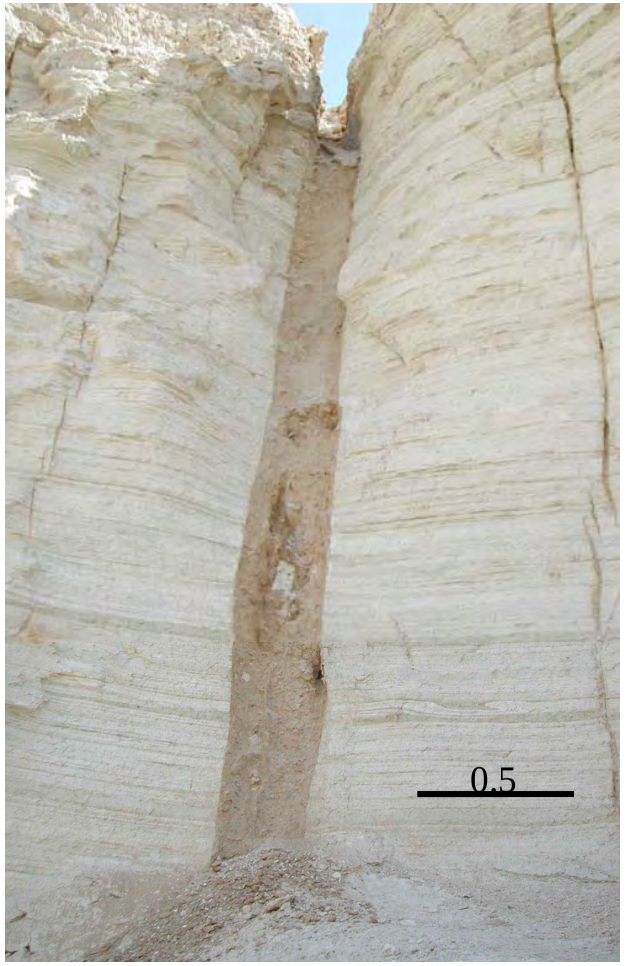

Figure 2: Clastic dike, sub-vertical, sheets of sediment within a host rock. While the common final geometry of these structures is everywhere similar and well defined, their mode of formation is ambiguous.

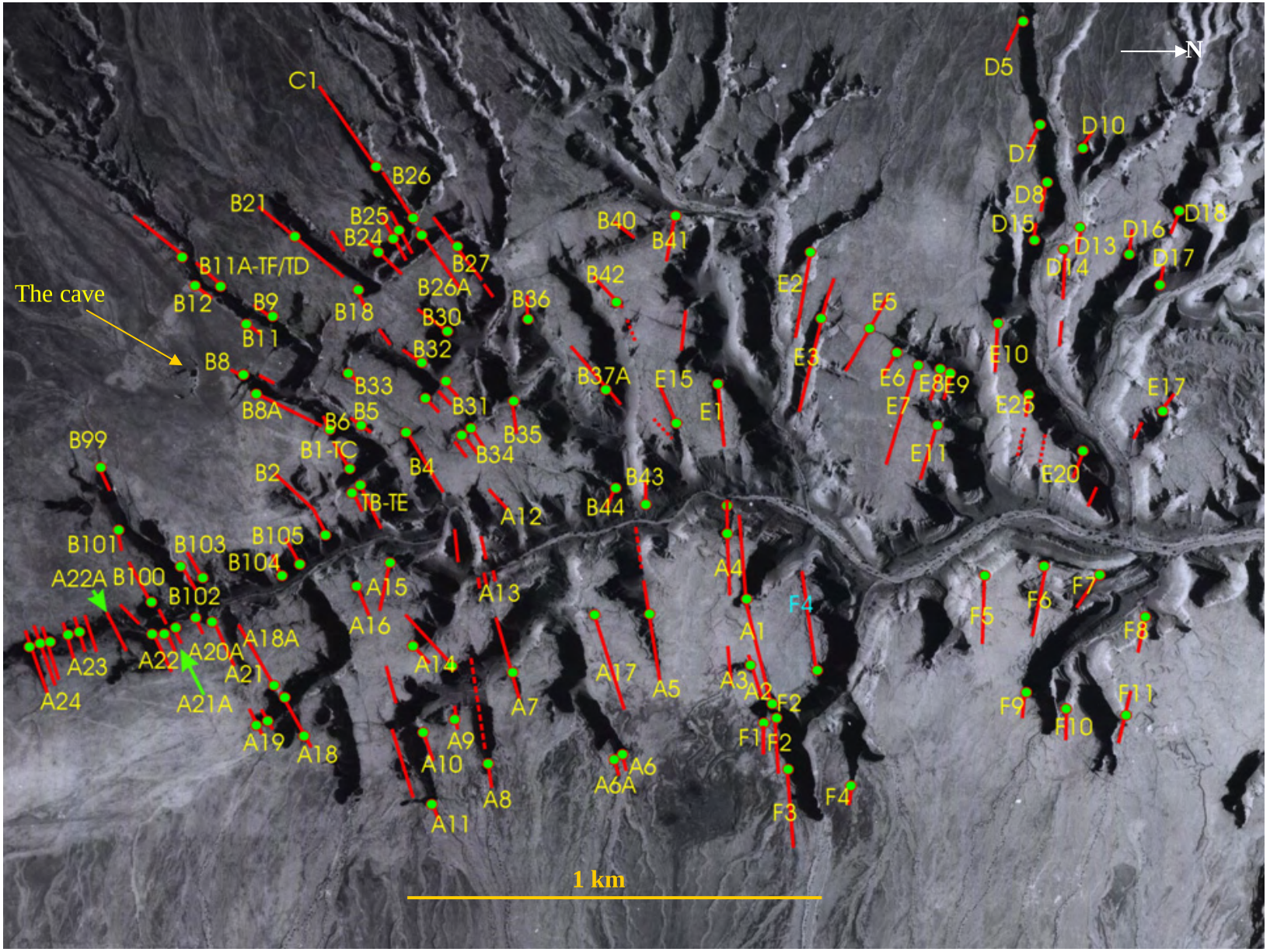

Figure 3: Location and geometry map of the clastic dikes that are arranged mainly in semi radial geometry (Marco et al 2002) in Ami'az Plain. The letter code denotes the dikes (after Levi et al., 2006a).

a) In injection dike

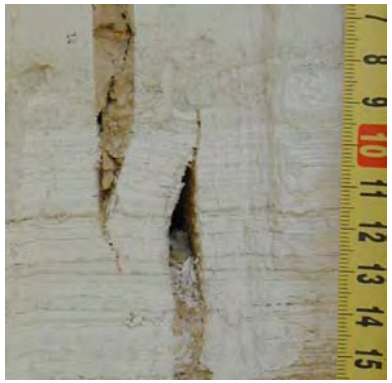

b) Segmented dike

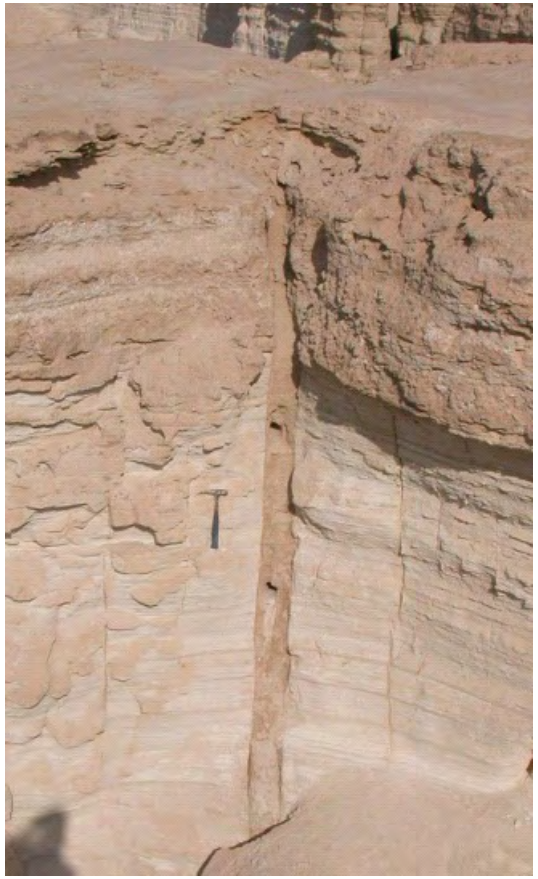

c) Sedimentary dike

Figure 4: Different transportation mechanism and fracturing style, during the clastic dike emplacement. a) Dike architecture resembles that of bifurcated dynamic fracture during upward propagation. b) Two disconnected, partially overlapping dike segments in the upper section of the Lisan Formation. Similar to magmatic dikes, this geometry hints at the role played by internal pressure during dike emplacement and horizontal transport of clastic material into the evolving dikes. Lisan laminae are not displaced along the dike walls, indicating that clastic dikes are extensional fractures. Note that because the dike segments are not physically connected to the surface, the flow within it had a lateral component. c) Wide (~0.4 m) sedimentary clastic dike open at surface filled with brownish silt. Source of fill is veneer of eolian and fluvial sediments, which cover Ami'az Plain (after Levi et al., 2006a).

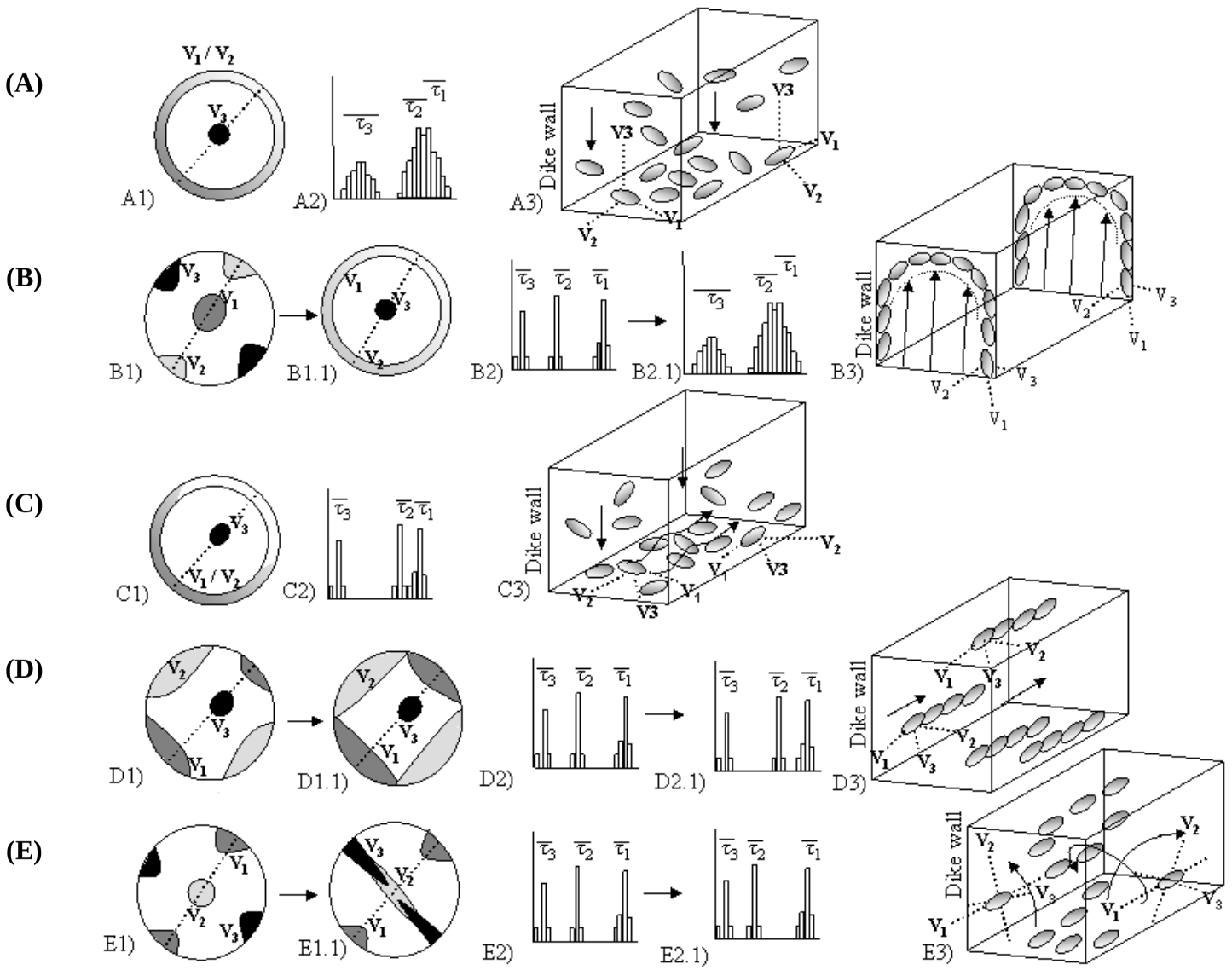

Figure 5: AMS for clastic dikes (synthetic models) that were emplaced under different conditions (after Levi et al, 2006b). (A) Sedimentary (oblate) AMS fabric in depositional dikes. (B) Flow AMS fabric developed during injection of viscous Newtonian fluid and characterized by imbrications along the dike's walls. (C) Low-energy flow fabric of oblate to weak triaxial AMS ellipsoids. (D) Moderate energy flow fabric of triaxial. (E) High-energy flow fabric of triaxial. The principal axes are either grouped (E1) or streaked (E1.1) due to rotation of particles during turbulent flow.

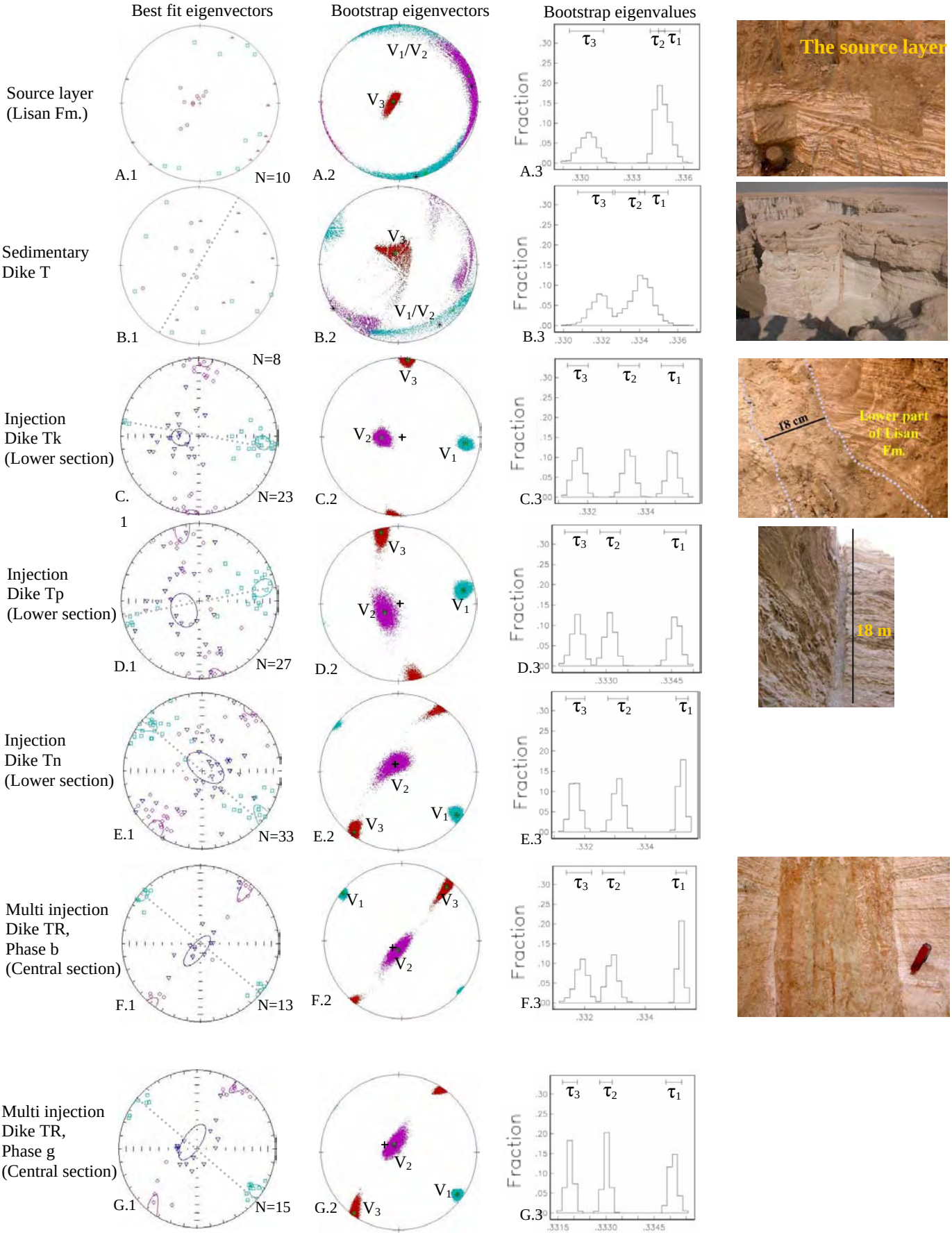

Figure 6: AMS of the source layer, sedimentary dike (Dike To, A) and five injection dikes (Dikes Tk, Tp, Tn, Tp, and TR). A1–G1: Lower-hemisphere, equal-area projections of AMS principal axes and the 95% confidence ellipses; squares represent V1 axes, triangles represent V2 axes, and circles represent V3 axes. A2–G2: Lower-hemisphere, equal-area projections of AMS principal axes analyzed by the bootstrapping method. A3–G3: Principal values distribution with 95% confidence bounds. Dashed lines mark the dike strike (after Levi et al., 2006a,b).

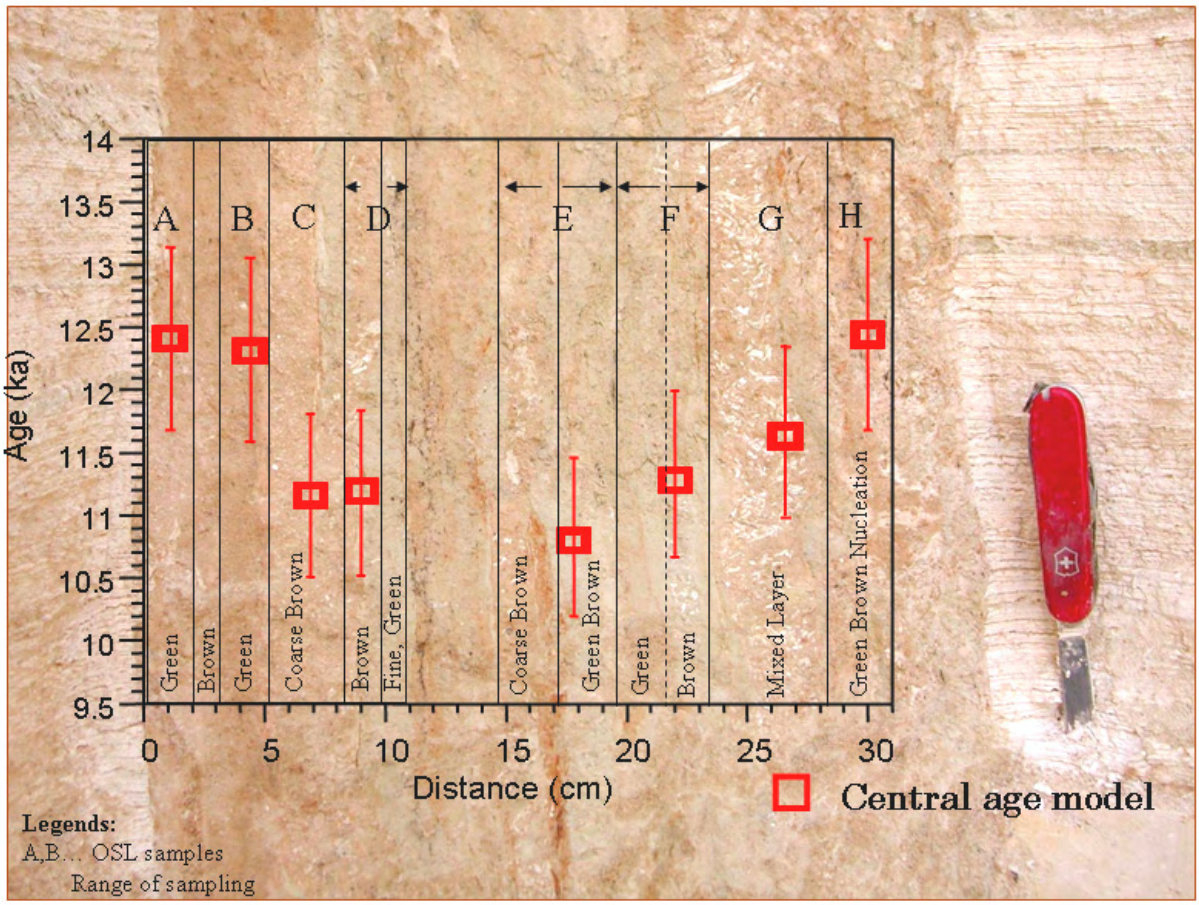

Figure 7: A multi-phase dike composed of 11-12 adjacent vertical sheets of sediment that can be differentiated based on their color and texture. We interpreted these sheets as discrete and separate episodes of injection phases, and hypothesized that the older phases would be closer to the dike margins. Eight individual phases and samples (A-H) are shown schematically. Note that some samples include more than one phase. The age for each sample is plotted as a function of distance from the left wall of the dike. Errors were calculated using the central age models. The uncertainties on the ages are large and all the ages overlap. The ages range between 12.3±1.1 ka and 10.9±0.9 ka indeed decrease towards the center of the dike. At least four injection episodes can be clearly distinguished, with only several hundred years difference between them (after Porat et al., 2007).

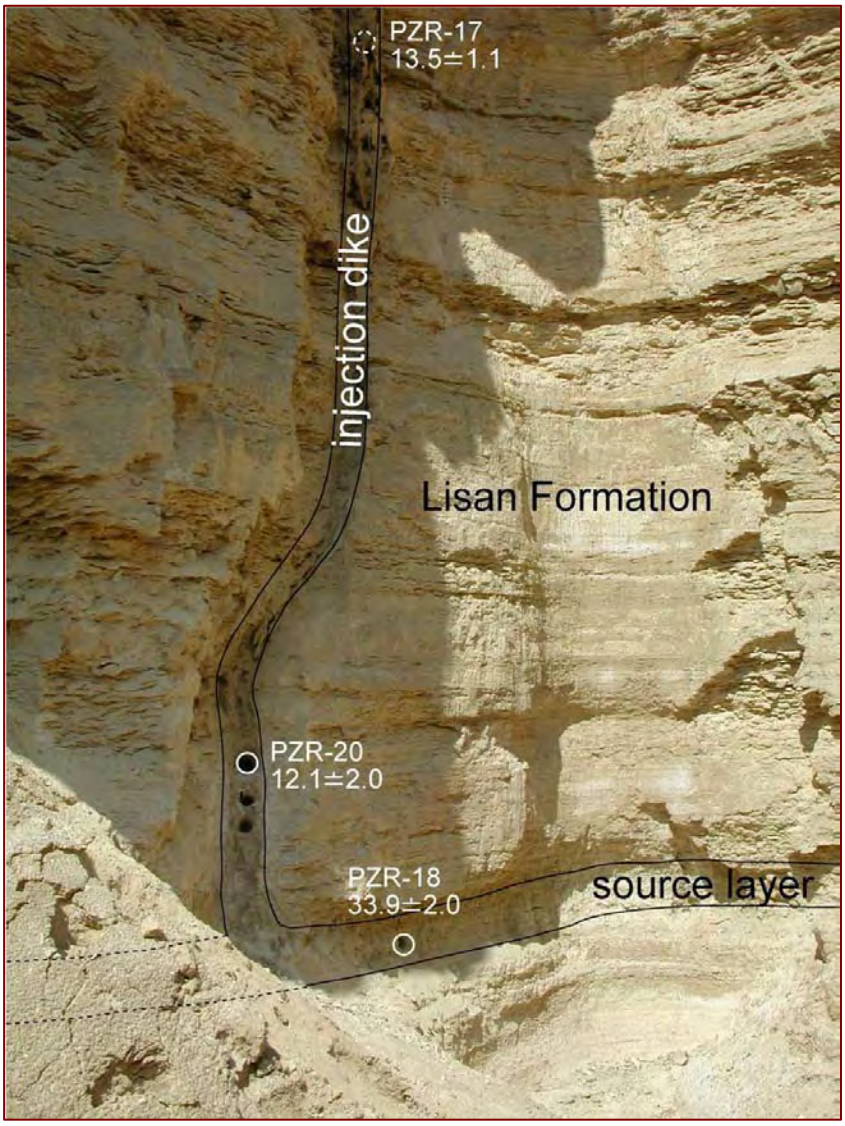

Figure 8: A source horizontal layer and a connected vertical injection dike sampled for OSL dating. Sample numbers and ages (in ka) are indicated. Upper sampling hole (broken line) is projected from a sampling site located ~30 m away along the dike strike. Width of sampling holes is ~ 8 cm. The age of the source layer agrees with U-Th ages for the Lisan Fm. However the OSL ages in the dike are much younger, indicating resetting of the OSL signal during injection (Porat et al., 2007).

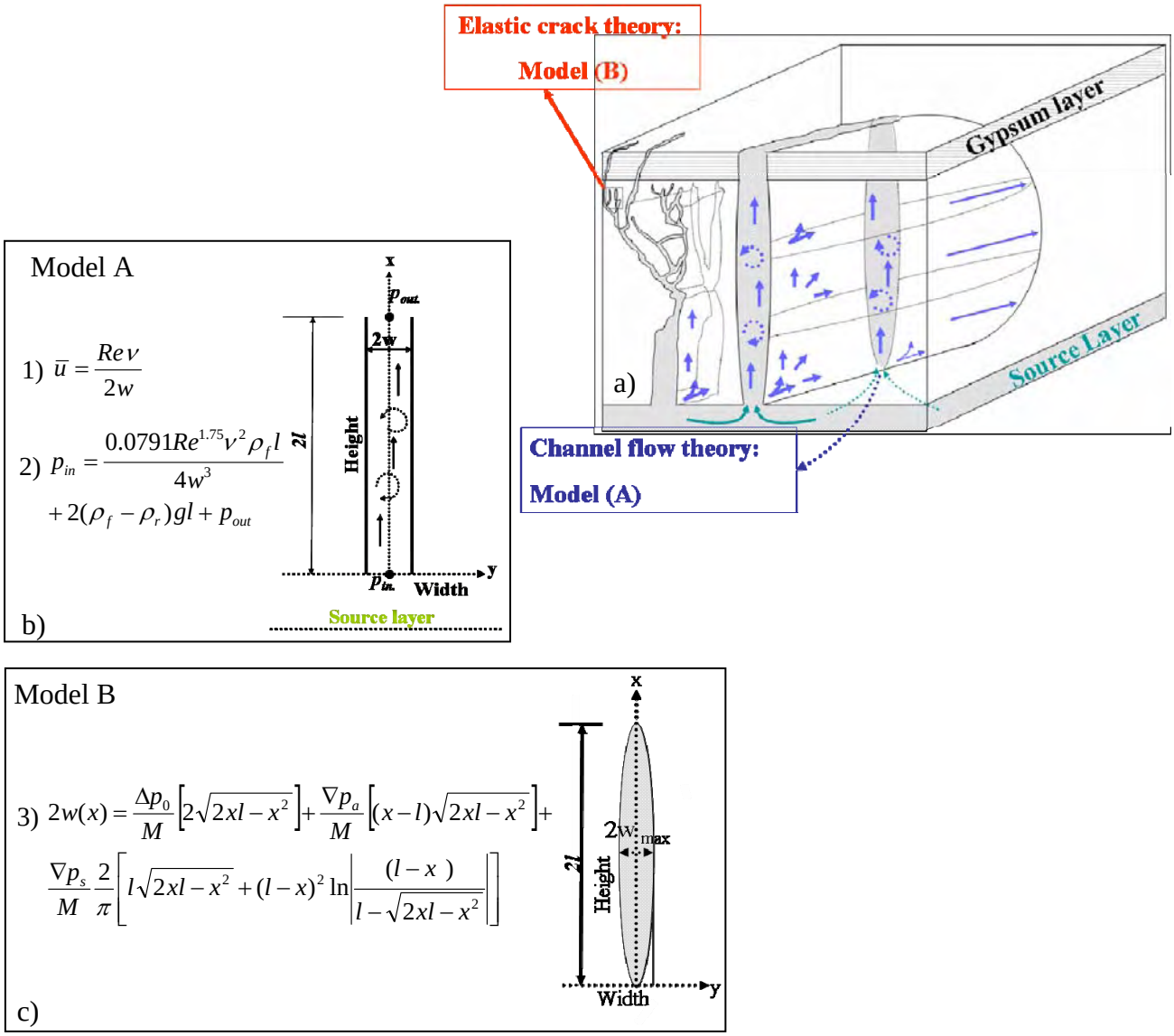

Figure 9: (a) Schematic representation of the two types of dikes: a blade-like dike with a cross section resembling a channel and a branching dike and its associated dikelets (left-hand panel). Some dikes/dikelets cross the upper stiff gypsum layer and some do not. (b) Model (A), showing upward flow along the *x*-axis under turbulent flow conditions. (c) Model (B), showing dilation profile of a representative dikelet. In Eq. (1) $\bar{u}$ is the mean velocity, *Re* is the Reynolds number, is the kinematic viscosity and *2w* is the dike width. In Eq. (2) P_{in} is the pressure at the source layer, $_f$ is the fluid density, $_r$ is the host rock density, g is the constant of gravitational acceleration and l is the half dike height. In Eq. (3), the general dilation profile solution, Δp_0 is the uniform normal stress, p_a is the asymmetric linear stress gradient, p_s is the symmetric linear stress gradient and M is the elastic stiffness (after Levi et al., 2008).

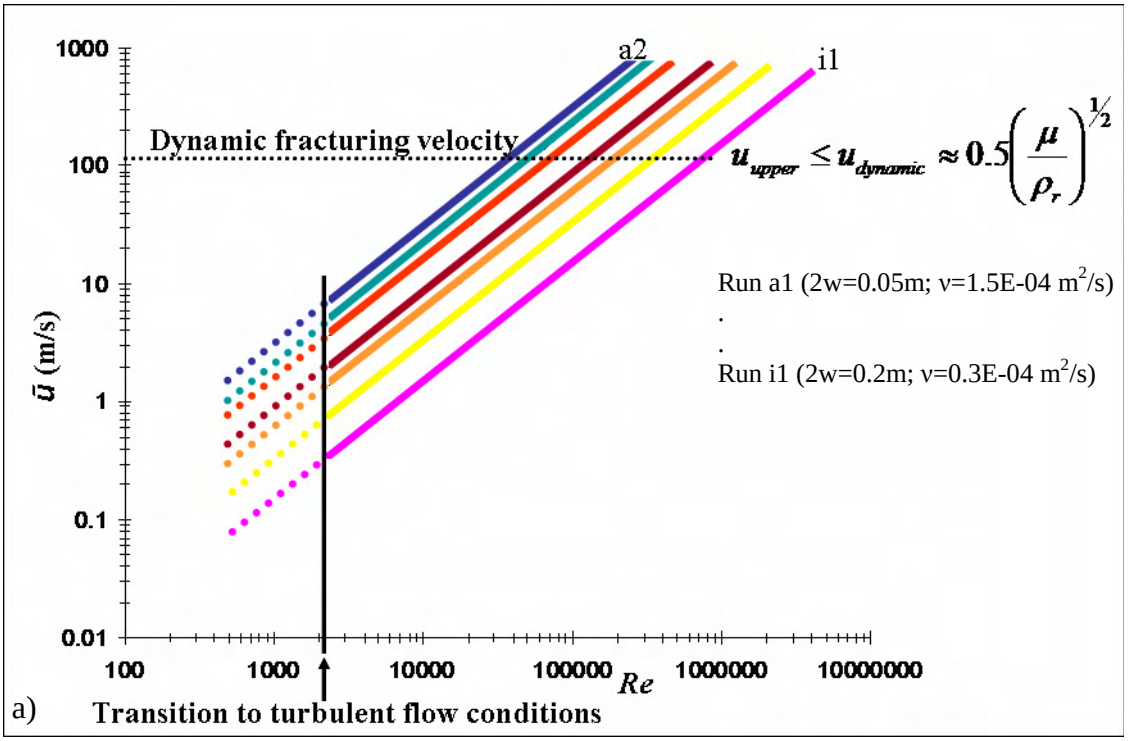

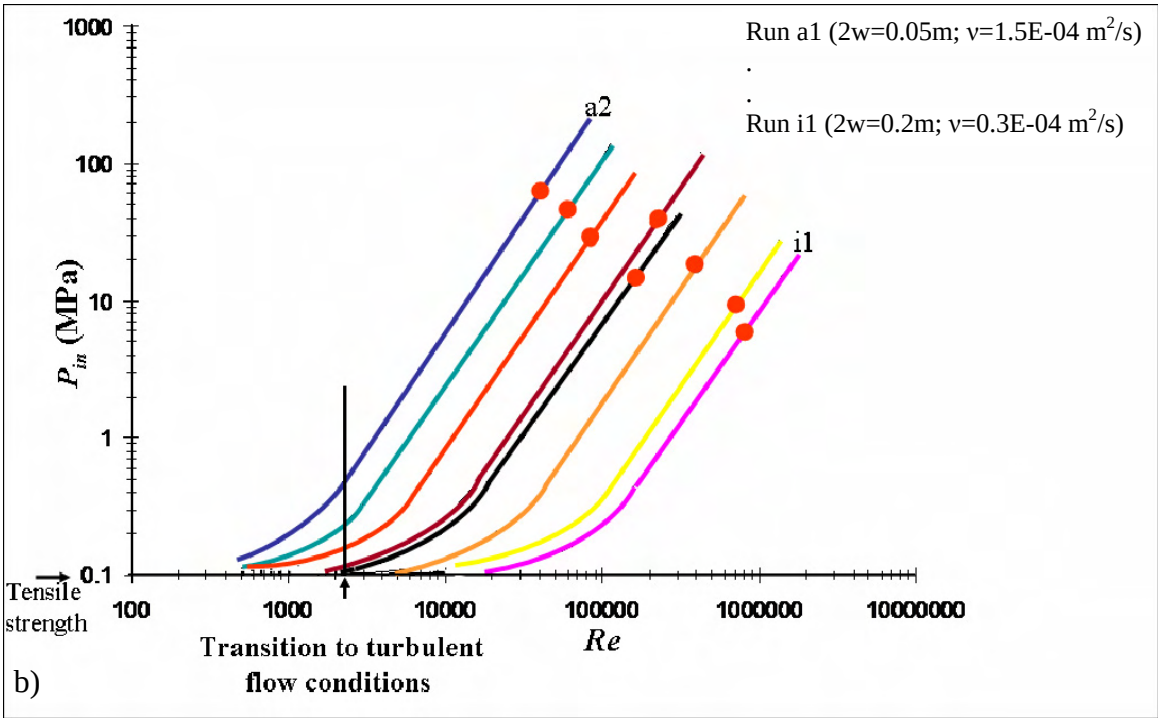

Figure 10: a) Results of model (B), showing the mean injection velocity as a function of *Re* plotted on log-log graph. b) Results of model (A), showing pressure at the source layer as a function of *Re* plotted on log–log graph. The red filled circles denote the possible upper pressures calculated by using the Reynolds numbers that are related to the high velocity values (after Levi et al., 2008). High velocity values, comparable to the dynamic fracture velocity.

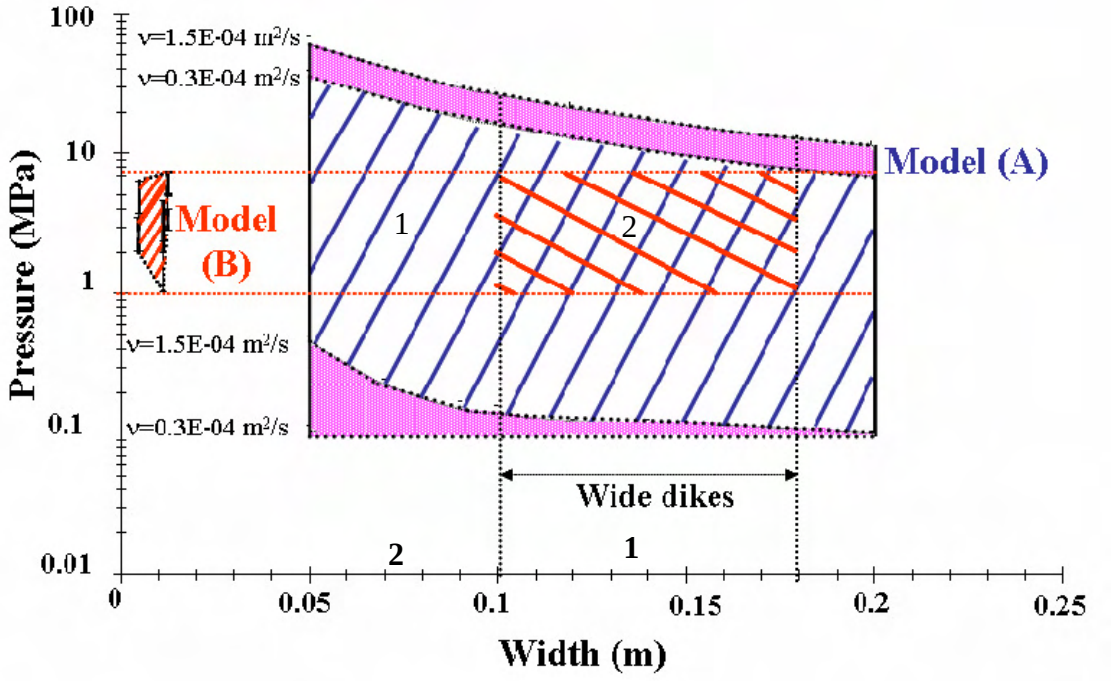

Figure 11: Range of possible pressures in the source layer versus the width of the clastic dikes calculated by coupling model (A) and model (B). The pink polygons mark the minimal and maximal pressures calculated using model (A) with kinematic viscosity ν = 0.3E – 04 m^2 s–1 and ν = 1.5E – 04 m^2 s–1. Bars correspond to the pressure range for each dikelet calculated using model (B). The polygon bounding these bars defines the estimated pressure range based on model (B). Polygons #1 and #2 represent the most probable range of driving pressures for wide and narrow dikes estimated by integrating models (A) and (B). The overlapping driving pressures of the two models are between 1 and 10 MPa. Based on the lower value of the driving pressure (1 MPa), the associated *Re* numbers were derived from Fig. 10b and, consequently, substituted them in Fig. 10a to obtain a lower value for the injection velocity of ~10 m/s. It is most likely that wider dikes, associated with large elastic deformations, were emplaced under higher driving pressures, probably generated by stronger seismic events or due to more efficient local pressure build-up in the source layer (after Levi et al., 2008).